Under-resolved gradients: slow wake recovery and low turbulence behind wind farms parameterized in mesoscale simulations

William C. Radünz[1], Jens H. Kasper[2], Richard J. A. M. Stevens[2], and Julie K. Lundquist[1,3]

[1]Johns Hopkins University, Baltimore, MD, USA
[2]Physics of Fluids Group, Max Planck Center for Complex Fluid Dynamics, J. M. Burgers Center for Fluid Dynamics, University of Twente, Enschede, the Netherlands
[3]National Laboratory of the Rockies, Boulder, CO, USA

Correspondence: William C. Radünz (wcorrea1@jh.edu)

Abstract. Numerical Weather Prediction (NWP) and climate models equipped with Wind Farm Parameterizations (WFPs) can simulate cluster wake effects affecting downstream wind farms in both onshore and offshore environments. This study evaluates the wake recovery behind a wind farm represented by the NWP-WFP approach in the Weather Research and Forecasting (WRF) model using either the Fitch et al. (2012) or Ma et al. (2022b, a) WFPs. Results are benchmarked against large-eddy simulations (LES) of an idealized offshore wind farm with aligned and staggered layouts under neutral atmospheric stability. The near-farm wake recovery is underestimated in NWP-WFP simulations because of two interconnected issues. First, the spatial gradients in the wind velocity field within the near-farm wake are necessarily under-resolved at mesoscale grid resolutions compared to the LES. Second, the low turbulence kinetic energy (TKE) in the near-farm wake in the mesoscale simulations is not due to excessive dissipation, but rather to insufficient shear production of TKE caused by these under-resolved gradients. As a result, a wind speed bias of approximately 0.15–0.60 m s^{-1} develops in the near-farm wake, depending on the simulation setup and wind-farm layout. Although this behavior is confined to a short downstream distance, it has lasting consequences for the far wake region. Furthermore, the slow near-farm wake recovery is not caused by a limitation of the WFP itself, but by the representation of inherently fine-scale processes on a coarse mesoscale grid. These results underscore the need to address under-resolved spatial gradients to improve wake recovery and reduce far-wake biases in NWP-WFP simulations.

1 Introduction

The sheer scale of offshore wind farms is attracting increasing attention from the scientific community (Barthelmie et al., 2007, 2009; Platis et al., 2018; Pryor et al., 2020; Cañadillas et al., 2020; Rosencrans et al., 2024; Ouro et al., 2025) largely due to cluster wake effects and associated power losses. The combination of massive wind farms ($\sim$1 GW), large turbines (10–20+ MW), and the relatively low turbulence offshore (Bodini et al., 2019) leads to strong, persistent wakes that can extend tens of kilometers downstream of the wind farms (Platis et al., 2018). As a result, inter-farm wake effects pose challenges not only to operating wind farms but also to those in planning or development stages, thus mirroring concerns already observed in onshore settings (Lundquist et al., 2019). Understanding and accurately predicting the wakes that arise from atmosphere–wind farm interactions is therefore of scientific and economic relevance (Veers et al., 2019, 2022). In this context, Numerical Weather Prediction (NWP) models equipped with Wind Farm Parameterizations (WFPs) are proving to be a valuable tool (Fischereit et al., 2022a).

The representation of wind farms in NWP and climate models has evolved significantly over the past two decades, moving from surface-based approximations to more physically realistic parameterizations. In the early 2000s, wind farms were incorporated into NWP and climate models through enhanced surface roughness (z_0) or drag (Ivanova and Nadyozhina, 2000; Malyshev et al., 2003; Keith et al., 2004; Wang and Prinn, 2010). However, this approach led to exaggerated surface fluxes, turbulence kinetic energy (TKE), and wind speed deficits (Fitch et al., 2013b). A key conceptual shift came with Baidya Roy et al. (2004), who proposed that wind farms act as an elevated momentum sink and TKE source within the rotor layer rather than at the surface. The elevated momentum sink and TKE source framework remains the conceptual foundation for most WFPs in use today, and for several subsequent advances (Fitch et al., 2012; Adams and Keith, 2013; Boettcher et al., 2015; Abkar and Porté-Agel, 2015; Volker et al., 2015; Pan and Archer, 2018; Redfern et al., 2019; Ma et al., 2022b). For a comprehensive overview of WFP developments, see the review by Fischereit et al. (2022a).

One of the key advances in WFPs was the modification of the TKE source term, initially treated as a constant (Baidya Roy et al., 2004). Blahak et al. (2010) proposed linking the added TKE to the energy extracted by the turbines via the power coefficient (C_P), and Fitch et al. (2012) introduced the formulation $C_{\mathrm{TKE}} = C_T - C_P$, where C_T is the thrust coefficient. Later, Archer et al. (2020) suggested scaling C_{TKE} with a TKE factor (α) of 0.25 to avoid exaggerated TKE values. Even though some studies find better performance using $\alpha =$ 1.00 instead (Larsén and Fischereit, 2021), the impact of changing α varies spatially (Rosencrans et al., 2024; Ali et al., 2023; García-Santiago et al., 2024). Most recently, large-eddy simulation (LES)-based formulations have been proposed to further improve the TKE source term (Khanjari et al., 2025).

Regarding the WFPs and the representation of atmosphere–wind farm interactions, it is useful to distinguish between grid-unresolved and grid-resolved processes. Unresolved processes include the momentum sink term, intra-grid-cell interactions between turbines (Abkar and Porté-Agel, 2015; Pan and Archer, 2018; Ma et al., 2022b), local wake expansion (Volker et al., 2015), and wake recovery occurring within the same grid cell. The momentum sink term creates a wind speed deficit (wake) as a grid-unresolved process. However, momentum recovery into the generated wake is a spatial process that occurs over several grid cells and depends on spatial gradients of wind speed, direction, TKE, in addition to planetary boundary layer (PBL) schemes. Wake recovery is therefore also a grid-resolved process. This grid-resolved wake recovery depends on multiple factors. Several studies have shown sensitivity to horizontal grid resolution (Mangara et al., 2019; Siedersleben et al., 2020; Tomaszewski and Lundquist, 2020; Peña et al., 2022; Sanchez Gomez et al., 2024) and vertical resolution (Vanderwende et al., 2016; Mangara et al., 2019; Tomaszewski and Lundquist, 2020; Siedersleben et al., 2020). The PBL scheme is also influential (Rybchuk et al., 2022; Agarwal et al., 2025), as is the tuning of the TKE addition factor α (Archer et al., 2020; Siedersleben et al., 2020; Tomaszewski and Lundquist, 2020; Larsén and Fischereit, 2021; Sanchez Gomez et al., 2024). In addition, atmospheric stability plays a key role in modulating wake recovery and has been highlighted in several recent works (Vanderwende et al., 2016; Lundquist et al., 2019; Rosencrans et al., 2024; García-Santiago et al., 2024; Quint et al., 2025). Performance also varies between different WFPs. For instance, the Explicit Wake Parameterization (EWP) generally produces shorter wakes than the Fitch scheme (Shepherd et al., 2020; Pryor et al., 2020; Larsén and Fischereit, 2021; Fischereit et al., 2022b; García-Santiago et al., 2024; Pryor and Barthelmie, 2024).

The underestimation of wake recovery in NWP-WFP simulations is related to grid-resolved processes. A conceptual description of the generation and recovery of the wake in NWP-WFP, in comparison with LES, is provided in Fig. 1. Two downstream cells are used because the added TKE in the LES usually reaches its maximum in the first downstream cell (Fig. 1e), whereas the added TKE maximum occurs at the turbine grid cell for the NWP-WFP (Fig. 1d). Thus, wake recovery and TKE decrease are assessed here as streamwise changes between two consecutive downstream cells (Figs. 1b and c; e and f). The NWP-WFP ΔWS barely changes between panels (Figs. 1b and c), whereas the LES displays recovery. On the other hand, the ΔTKE decreases too fast for the NWP-WFP compared with the LES between panels (Figs. 1e and f). Because the slow wake recovery and the abrupt TKE decrease in the NWP-WFP occur in downstream cells without turbines, they may not be caused by the WFP.

Multiple NWP-WFP studies report good agreement of the wind speed deficit with LES within turbine or farm grid cells (Abkar and Porté-Agel, 2015; Vanderwende et al., 2016; Peña et al., 2022; García-Santiago et al., 2024), suggesting that the momentum sink term (i.e., the grid-unresolved component) creates a wind speed deficit consistent with the LES (Fig. 1a). However, after the generation of the wind speed deficit, the downstream wind speed profiles often remain unchanged in the NWP compared to the LES (Figs. 1b and c). This discrepancy in wake recovery between NWP-WFP and LES persists across neutral, convective, and stable atmospheric stability regimes (García-Santiago et al., 2024). Ultimately, this slow recovery in NWP-WFP simulations likely contributes to the overestimation of power losses often reported when using WFPs (Lee and Lundquist, 2017; Montavon et al., 2024). In Montavon et al. (2024), additional factors affecting turbine power estimates are identified, including the absence of a turbine induction correction in the standard Fitch WFP, which was subsequently addressed by Vollmer et al. (2024). Thus, the evidence of a well-functioning momentum sink term combined with the insufficient wake recovery downstream of turbine grid cells suggests the problem could be in the grid-resolved wake recovery process.

However, several studies using NWP-WFP simulations driven by realistic synoptic conditions have reported reasonable agreement between simulated and observed wind speed deficits in wind farm wakes. Such agreement has been demonstrated using aircraft measurements (Siedersleben et al., 2018a, b, 2020; Larsén and Fischereit, 2021; Ali et al., 2023; van Stratum et al., 2022) as well as SCADA data (Sanchez Gomez et al., 2024) in offshore wind farms. The contrast between idealized

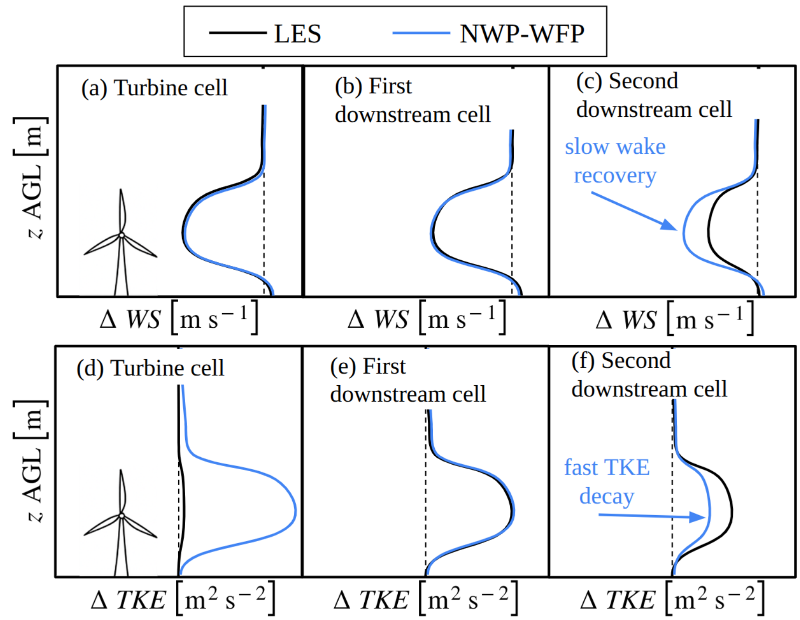

Figure 1. Conceptual description of wind turbine wake generation and recovery in a NWP-WFP simulation provided as a summary of the literature (Abkar and Porté-Agel, 2015; Vanderwende et al., 2016; Peña et al., 2022; García-Santiago et al., 2024). Time-averaged vertical profiles of wind speed deficit (ΔWS, a–c) and turbine-added TKE (ΔTKE, d–f) within the turbine grid cell (a, d), for the first (b, e) and second (c, f) downstream cells in the NWP without turbines. The wind speed deficit is defined as the difference between simulations with and without turbines ($\Delta WS = WS_T - WS_{NT}$), respectively, yielding negative values in most of the wake. The turbine-added TKE ($\Delta TKE = TKE_T - TKE_{NT}$) is similarly defined but typically yields positive values.

NWP-WFP simulations evaluated against LES, which can exhibit slower wake recovery, and realistic NWP-WFP simulations validated against observations motivates further investigation. It remains unclear whether the slower wake recovery in idealized configurations arises from limitations of the WFP itself or from deficiencies in the representation of wake recovery on a mesoscale grid. Clarifying this distinction is essential for assessing when NWP-WFP simulations can reliably represent wake evolution and associated power losses, and constitutes the central motivation of this study.

Another issue, less frequently discussed, is the rapid decrease of farm-induced TKE in NWP-WFP simulations. While less obvious, this problem is evident when closely examining the spatial evolution of TKE profiles downstream of turbine grid cells. In NWP-WFP simulations, TKE decreases more rapidly than in LES, as conceptually illustrated in Figs. 1e and f, and supported by evidence from the literature (Figs. 5a–d in Vanderwende et al. (2016); Figs. 4 and 9 in García-Santiago et al. (2024); Figs. 11-13 in Peña et al. (2022)). As more studies focus on wake recovery in large farms, this issue is becoming more visible. For example, Rosencrans et al. (2024) found that the amount of TKE added by the farm influences near-farm wake deficits but not the overall wake length. Similarly, Sanchez Gomez et al. (2024) noted that wake losses at an offshore wind farm located approximately 15 km downstream of another farm were largely unaffected by the TKE factor. However, omitting the

TKE factor ($\alpha = 0$) resulted in the largest biases when compared with SCADA data. Furthermore, aircraft observations have shown that TKE is overestimated in the first half of the farm by NWP-WFP, while in reality, TKE peaks further downstream (Siedersleben et al., 2020).

These two interrelated issues—the underestimated wake recovery and the fast decrease of the farm-added TKE—need a closer examination. While introduced here as two separate problems, turbulent mixing is a key driver for wake recovery (Vermeer et al., 2003; Abkar and Porté-Agel, 2015; van der Laan et al., 2023; Kasper and Stevens, 2026). Unrealistic decrease of the TKE can slow down wake recovery in NWP-WFP simulations. Therefore, these two issues raise a few important questions. For instance, why does the farm-added TKE decrease more quickly in NWP-WFP simulations than in the LES? How much does this rapid decrease contribute to the underestimated wake recovery? What other physical or numerical factors are involved? To address these questions, we evaluate the representation of wind farm wake recovery in the NWP-WFP approach. Specifically, we aim to quantify the magnitude and spatial variability of the recovery process behind a wind farm and identify the mechanisms behind the underestimation. This effort requires a large-domain LES to evaluate wake recovery within, immediately downstream and in the far wake of the wind farm. To our knowledge, there are no NWP-WFP vs. LES comparisons over downstream distances of $\sim$40 km.

The remainder of this article is structured as follows. Section 2 describes the numerical setups used in this study, including the WRF simulations with the Fitch (Fitch et al., 2012) and MAV (Ma et al., 2022b, a) wind farm parameterization (NWP-WFP) and the reference LES with actuator disks (Kasper et al., 2024). The idealized simulations focus on a 600 MW offshore wind farm with aligned and staggered layouts, subjected to westerly flow under near-neutral atmospheric conditions. In Section 3, we compare the undisturbed inflow conditions across models to ensure consistency. We then assess wind farm performance and analyze wake recovery in the streamwise direction. Section 4 discusses in depth the two main limitations of wake recovery in mesoscale simulations using WFPs: the fast decrease of farm-added TKE and the under-resolved gradients in the wind farm wake. Finally, Section 5 summarizes the key findings, with particular emphasis on how these limitations impact the simulation of wind farm cluster wakes with NWP-WFP models.

2 Methods

To benchmark the NWP simulations with the WFP, we compare the results against LES by Kasper et al. (2024), who studied atmosphere–wind farm interactions under idealized conditions. Specifically, we consider the Barotropic (BT) case of their study, which here serves as the reference case that the mesoscale NWP simulations are designed to replicate. The simulation setup for this LES is briefly covered in Section 2.1, while a thorough discussion on the numerical framework can be found in Kasper et al. (2024). The subsequent Section 2.2 details the NWP-WFP framework, and the adaptations required to represent the LES conditions within a mesoscale model.

2.1 Setup for the LES

The reference simulation uses a modified version of the LES code developed by Albertson and Parlange (1999), later validated in Gadde et al. (2021). The model solves the incompressible filtered mass conservation, Navier–Stokes, and potential temperature transport equations. The subgrid-scale stresses and heat fluxes are modeled using the anisotropic minimum dissipation (AMD) scheme (Rozema et al., 2015; Abkar et al., 2016a), suitable for stratified boundary layers and wind farm wakes.

In the horizontal directions, the code employs pseudo-spectral differentiation and periodic boundary conditions, while second-order finite differencing is used in the vertical direction. A free-slip boundary condition is imposed at the top, with a Rayleigh damping layer to minimize gravity wave reflections. At the surface, a zero heat flux condition enforces neutral stratification, and shear stresses are parameterized using Monin–Obukhov similarity theory. Time integration uses a third-order Adams–Bashforth scheme. The simulation domain spans $102.4 \times 10.24 \times 10\,\mathrm{km}^3$ in the streamwise, spanwise, and vertical directions, respectively. It is discretized using a rectilinear grid that consists of $2048 \times 512 \times 384$ points, with horizontal resolutions of $\Delta x = 50$ m and $\Delta y = 20$ m. In the vertical, the resolution is uniform with $\Delta z = 10$ m up to $z_u = 1.5$ km above ground level (AGL), and stretched above using a hyperbolic tangent profile up to a maximum spacing of 62 m.

The simulated atmosphere represents an idealized offshore environment based on North Sea conditions. The geostrophic wind vector is prescribed with a magnitude $|\mathbf{U}_g| \approx 10\,\mathrm{m\,s^{-1}}$, and the Coriolis frequency equals $f_c = 1.159 \times 10^{-4}\,\mathrm{s^{-1}}$. The surface roughness is set to $z_0 = 0.002$ m, typical for open-sea conditions. The background stratification is neutral up to 1 km AGL, with a potential temperature of $\theta = 286$ K. The boundary layer is capped by a 3 K inversion over 200 m, followed by a free-atmosphere lapse rate of 5 K km^{-1}.

Two sets of LES are considered, representing aligned and staggered wind-farm layouts. Wind turbines are represented using the actuator disk model (Jimenez et al., 2008; Calaf et al., 2010). The simulated wind farm consists of ten rows and six columns of turbines arranged in an aligned layout configuration, spaced by $s_x = 7D$ and $s_y = 5D$ in the streamwise and spanwise directions, respectively. A staggered layout configuration is also considered, with an additional spanwise displacement of $2.5D$ between successive rows. The turbine diameter equals $D = 178$ m and the hub-height $z_h = 119$ m AGL, corresponding to the DTU 10-MW reference turbine (Bak et al., 2013). A uniform thrust coefficient $C_T = 0.75$ is used, and turbines yaw to face the local incoming wind.

Each LES is run for a total of 11 hours and comprises two stages. First, a 7-hour spin-up simulation is run on a coarser grid with a resolution of $2\Delta_x \times 2\Delta_y \times \Delta_z$. Second, once the boundary layer reaches quasi-equilibrium (the mean wind and turbulence statistics display small variations over time), it is interpolated to the full resolution and the LES proceeds as a precursor-successor simulation (Stevens et al., 2014). The precursor provides realistic turbulent inflow to the successor domain containing the wind farm, preventing contamination of the inflow by remnants of the wakes via the periodic boundary conditions. Statistics are then collected over the final 3 hours of the simulation.

2.2 Setup for the NWP-WFP simulations

The NWP simulations use the Advanced-Research WRF model version 4.4 (Skamarock et al., 2019), which solves the compressible Euler equations in three spatial dimensions and time. The solver uses a time-split integration scheme. The low-frequency modes are integrated with a third-order Runge–Kutta scheme, whereas higher-frequency acoustic modes are integrated over smaller time steps. Advective terms are discretized using a fifth-order scheme in the horizontal and a third-order scheme in the vertical directions. The model applies Arakawa C-grid staggering in the horizontal direction, with a hydrostatic pressure-based coordinate in the vertical direction.

Idealized simulations are employed, omitting cloud microphysics, radiation, moisture, and surface heterogeneity, which are standard simplifications in studies targeting canonical boundary layers over flat terrain (Fitch et al., 2012; Vanderwende et al., 2016; Volker et al., 2015; Peña et al., 2022; García-Santiago et al., 2024). In the multiscale framework of the WRF model, turbulence is entirely parameterized by the PBL scheme for mesoscale grid spacings ($\Delta X \sim 1$ km). Vertical turbulent mixing is represented by the MYNN PBL scheme (Nakanishi and Niino, 2009; Olson et al., 2026), while horizontal mixing is treated using a two-dimensional first-order Smagorinsky closure with constant eddy diffusivity (Skamarock et al., 2019). In MYNN, TKE is prognosed from a budget equation that includes shear production, buoyancy production or destruction, vertical turbulent transport, and dissipation (Nakanishi and Niino, 2009; Olson et al., 2026). The diagnosed TKE is then used to compute eddy diffusivities through stability-dependent mixing-length formulations, which directly control the vertical transport of momentum and scalars in the PBL. Since vertical turbulent transport dominates near-farm wake recovery (Lanzilao and Meyers, 2025; Kasper and Stevens, 2026), the discussion here primarily reflects the role of the PBL scheme and grid-resolved dynamics in governing vertical mixing and shear-driven entrainment.

A two-domain nesting configuration is adopted (Fig. 2), with one-way coupling from a parent domain to an inner nest. The outer domain generates nearly steady boundary-layer inflow characteristics, which are passed to the nested domain. Both domains use a constant horizontal resolution ($\Delta X = \Delta Y$), hereafter referred to simply as ΔX, as specified in Table 1, ranging from 346 m to 1246 m for the sets of simulations considered here. Simulations with the finest horizontal grid resolutions ($\Delta X = 2D$, or 346 m, DX2D and DX2DTKE100) use a coarser resolution ($\Delta X = 5D$, 890 m) for the outer domain, with a parent grid aspect ratio of 3. Vertically, a fine 10-m resolution is used below 400 m AGL for all domains, resolving the turbine rotor layer with multiple grid points. The computational domain is larger than in the LES to further minimize the influence of lateral boundaries, as the added computational cost is relatively small for the NWP-WFP simulations. For most cases (except DX2D and DX2DTKE100) the innermost domain spans approximately 188 km streamwise and 63 km spanwise. In the finest-resolution cases (DX2D and DX2DTKE100), it spans about 100 km and 40 km in the streamwise and spanwise directions, respectively. All domains extend 5 km vertically.

The wind farm is represented using the Fitch (Fitch et al., 2012) and MAV (Ma et al., 2022b, a) WFPs, with TKE advection enabled (Archer et al., 2020) and axial induction modified following Vollmer et al. (2024). The wind farm consists of 60 DTU 10-MW turbines (Bak et al., 2013), configured identically to Kasper et al. (2024). Each turbine has a rotor diameter $D = 178$ m and a hub height $z_h = 119$ m AGL. A constant thrust coefficient of $C_T = 0.75$ is used in all cases, except for those included in

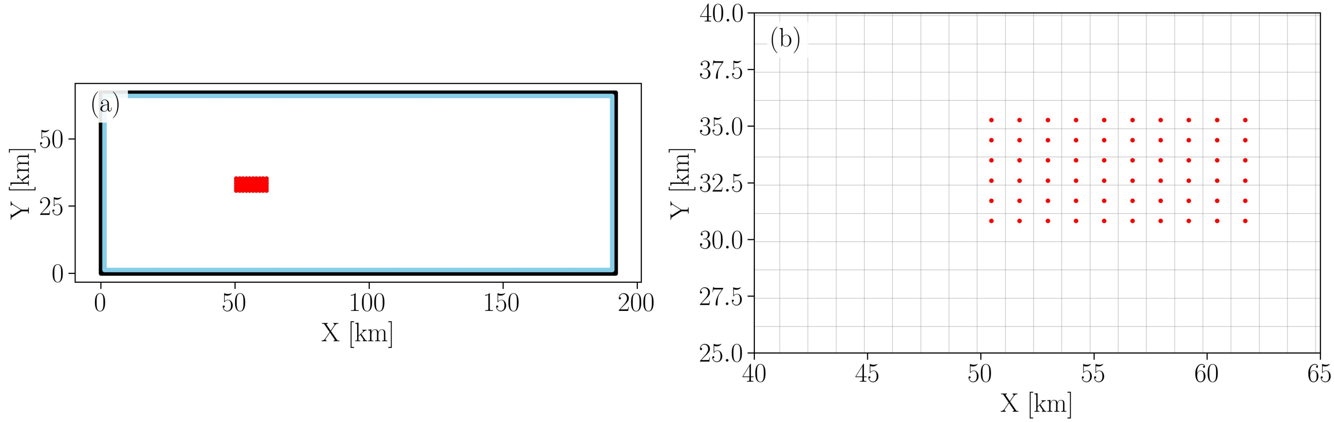

Figure 2. Two computational domains are used in the WRF-WFP simulations, illustrated here for the baseline (BASE) case (a). The outer parent domain (D1, black rectangle), which uses periodic lateral boundary conditions and does not include a wind farm, provides inflow to the inner nested domain (D2, blue rectangle) via one-way nesting. The inner domain includes the wind farm, with turbines represented as red dots. In the BASE setup shown in panel (b), each grid cell contains one turbine, except for the cells between Y =32–34 km, which contain two.

Table 1. Summary of the NWP-WFP simulations, their subsets and key parameters: horizontal grid resolution (ΔX), TKE addition coefficient (α), WFP and turbine thrust coefficient (C_T).

Case	Subset	ΔX [m]	α	C_T
BASE	Baseline	1246 (7D)	0.25	0.75
TKE000	TKE	1246 (7D)	0.00	0.75
TKE050	TKE	1246 (7D)	0.50	0.75
TKE075	TKE	1246 (7D)	0.75	0.75
TKE100	TKE	1246 (7D)	1.00	0.75
DX5D	Grid	890 (5D)	0.25	0.75
DX2D	Grid	346 (2D)	0.25	0.75
DX2DTKE100	Grid	346 (2D)	1.00	0.75
MAV	WFP	1246 (7D)	0.25	0.75
MAVDX12D	WFP	2076 (11.6D)	0.25	0.75
CT050	Thrust	1246 (7D)	0.25	0.50
CT081	Thrust	1246 (7D)	0.25	0.81
CTTC	Thrust	1246 (7D)	0.25	Thrust Curve (TC)

the C_T sensitivity study. Details on the turbine model and the sensitivity analysis are provided in Appendix A. The NWP-WFP simulations consider only the aligned wind farm layout. Because the coarser-resolution Fitch cases (BASE, TKE100) spatially over-distribute the wind speed deficit, the aligned configuration represents a worst-case scenario in terms of wake effects; accordingly, the staggered LES is also used as a reference for comparison with these coarser Fitch simulations.

The wind farm occupies a region starting around $X = 50$ km and $Y = 30$ km from the western and southern boundaries. The wind farm spans 11 km streamwise and 4.4 km spanwise, with turbine spacing of $7D$ (1246 m) in the streamwise and $5D$ (890 m) in the spanwise directions. Uniform turbine spacing in the coarse NWP-WFP grid is only achieved with Fitch when grid spacing matches the physical turbine spacing. For instance, the BASE case has a uniform horizontal spacing which ensures a uniform representation of turbine spacing in the streamwise direction ($\Delta X = S_x = 7D$), but not in the spanwise direction where turbines are more closely spaced ($\Delta X = 7D$ but $S_y = 5D$).

To investigate the role of subgrid wake effects on wake recovery, we additionally implemented the "MAV" wind farm parameterizations (Ma et al., 2022b, a), ported from the standard release of WRF v4.6. The MAV WFP is based on the analytical wake model of Xie and Archer (2015) and represents wake overlap through a superposition of hub-height wind speed deficits (Ma et al., 2022a). In contrast to the Fitch scheme, which relies on grid-cell-averaged momentum extraction, MAV explicitly accounts for subgrid wake interactions and has been shown to improve turbine power predictions when compared against offshore SCADA data (Ma et al., 2022a).

Surface boundary conditions assume flat, homogeneous terrain with roughness length $z_0 = 0.002$ m and zero surface heat flux (neutral stability). The surface-layer scheme applies Monin-Obukhov Similarity Theory (MOST)-based drag using near-surface wind speeds. The Coriolis parameter corresponds to a latitude of 52.65°. The upper boundary enforces zero vertical velocity and free-slip horizontal flow. A Rayleigh damping layer (coefficient 0.2 s^{-1}) occupies the top 2 km of the domain to absorb gravity waves.

Initial conditions prescribe a uniform, westerly flow from 282° at 10.93 m s^{-1}. The initial potential temperature is uniform at 286 K below 1000 m AGL, then increases with lapse rates of 15 K km^{-1} (1000–1200 m AGL) and 5 K km^{-1} (above 1200 m to the 5-km AGL domain top) to match the LES. Simulations run for 27 hours, with the final hour used for analysis after a 26-hour spin-up. The initial forcing is fine-tuned to ensure post-spin-up conditions match target values, a standard approach in idealized WRF setups (Mirocha et al., 2018; Peña et al., 2021; Hsieh et al., 2025). Inertial oscillations driven by Coriolis effects also modulate boundary-layer winds during spin-up. The chosen spin-up time ensures minimal residual oscillations in the analysis period.

Three simulation sets and a baseline case are run (Table 1). The baseline (BASE) case uses a horizontal resolution equal to the turbine streamwise spacing ($7D$) to avoid subgrid wake effects from multiple turbines in one cell. It applies a thrust coefficient of $C_T = 0.75$ (such as in (Kasper et al., 2024)) and a TKE addition coefficient of $\alpha = 0.25$ (Archer et al., 2020). The TKE subset includes $\alpha = 0.00$, 0.50, 0.75 and 1.00. The grid subset varies ΔX between 346 m ($2D$) and 890 m ($5D$). The thrust subset applies constant C_T values of 0.50 and 0.81, and also includes a wind-speed-dependent thrust case (see Appendix A). This subset serves to assess the sensitivity of the wake generation and recovery relative to the choice of $C_T = 0.75$ in the LES. The high-resolution cases DX2D and DX2DTKE100 are used to assess the impact of sharper wake gradients on power and recovery, acknowledging limitations of the application of traditional PBL schemes at sub-kilometer resolutions due to the *terra incognita* (Wyngaard, 2004; Rai et al., 2019; Haupt et al., 2019, 2023).

3 Results

3.1 Undisturbed inflow profiles

Before delving into modeling differences and similarities between NWP-WFP and LES in terms of power production and wake recovery, it is necessary to evaluate inflow variability to ensure inflow profiles are sufficiently similar so that downstream differences are not attributed to inflow variability (Peña et al., 2022; Hsieh et al., 2025). There is excellent agreement between NWP-WFP and LES inflow profiles for all variables (Fig. 3). The differences in hub-height (WS_{119}) and rotor-averaged (WS_r) wind speed compared to the LES are approximately 0.03 and -0.01 m s^{-1}, respectively, as shown in Table 2.

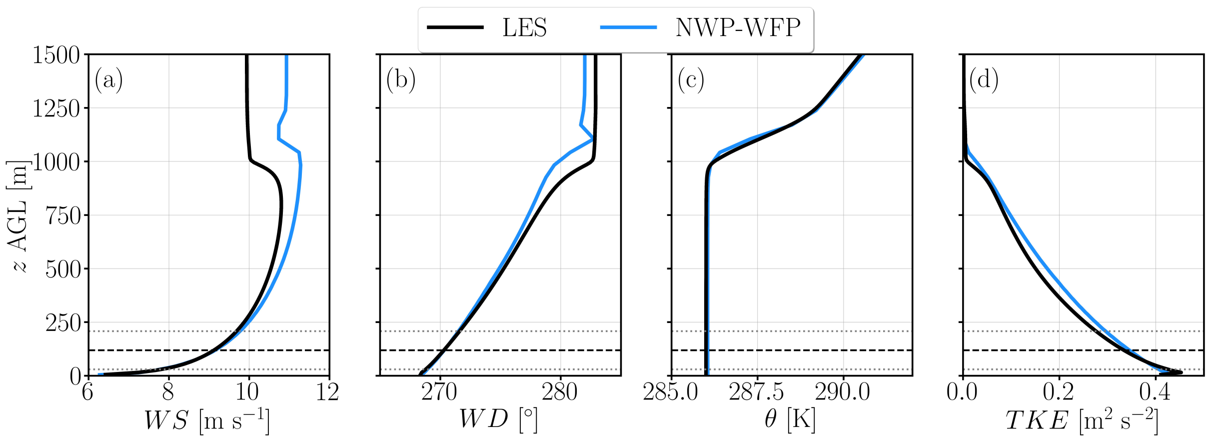

Figure 3. Time- and horizontally-averaged profiles of wind speed (a), wind direction (b), potential temperature (c), and TKE (d) during the analysis window for LES (black line) and NWP-WFP (blue line) in the simulation without turbines. The horizontal dashed and dotted gray lines denote rotor hub height and bottom/top tips, respectively.

Not only do the hub-height and rotor-averaged values match well, but so do the wind shear (α_r) and veer (β_r) across the rotor (Figs. 3a, b). This is important because under near-neutral conditions, turbulence production is governed primarily by mechanical shear, both in wind speed and direction (Stull, 1988). The fact that similar wind speed and direction profiles result in similar TKE profiles (Fig. 3d) reinforces the physical consistency between the models. The NWP-WFP wind speed profile exhibits slightly greater shear between 300 and 800 m AGL, which leads to marginally higher TKE values in that layer. Surface boundary conditions are also consistent, as indicated by the good agreement in friction velocity ($u_\star$, Table 2).

3.2 Row-averaged streamwise power patterns

This section evaluates streamwise changes in row-averaged power (i.e., averaged across turbines within the same row) for the TKE (Fig. 4a) and grid resolution (Fig. 4b) simulation subsets. These results reflect both the magnitude of wake effects owing to momentum extraction by the turbines and the ability of this waked flow to recover momentum within the wind farm.

Table 2. Time-averaged inflow properties from the precursor simulations and their differences. Subscripts 119 and r denote hub-height (in m AGL) and rotor-averaged values, respectively. For wind shear (ΔWS_r) and veer (ΔWD_r), values represent the difference between the top and bottom rotor tips.

Source	WS_{119} [m s^{-1}]	WD_{119} [°]	TKE_{119} [m^2 s^{-2}]	WS_r [m s^{-1}]	WD_r [°]	TKE_r [m^2 s^{-2}]	$u_\star$ [m s^{-1}]	ΔWS_r [m s^{-1}]	ΔWD_r [°]
NWP-WFP	9.15	270.3	0.35	9.02	270.3	0.35	0.32	1.98	2.58
LES	9.12	270.3	0.33	9.03	270.3	0.34	0.33	1.87	2.81
Difference	0.03	0.0	0.01	-0.01	0.0	0.01	-0.01	0.12	-0.23

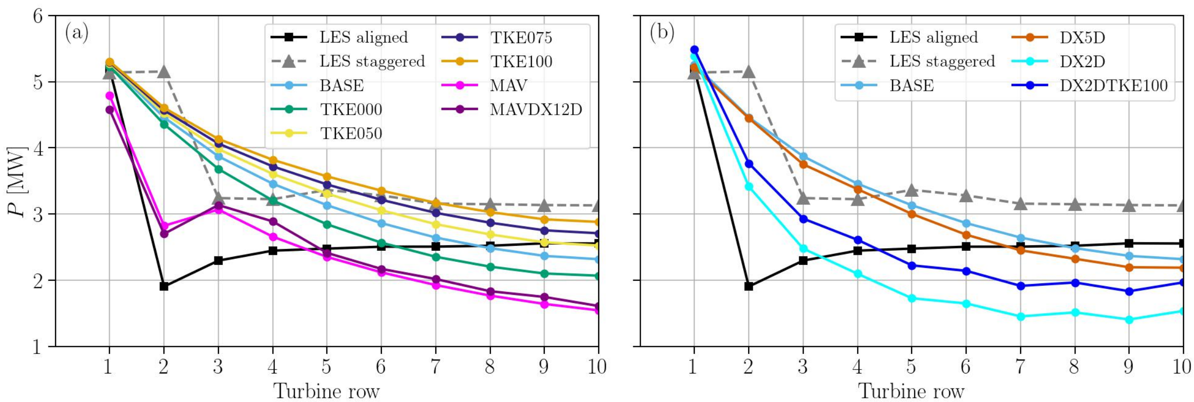

Figure 4. Row-averaged power in the NWP-WFP set of simulations with different wind farm added TKE and WFP (a) and grid resolutions (b) compared with the LES.

Compared to both the aligned and staggered LES, there is excellent agreement in the first-row averaged power output (∼5 MW; Fig. 4a), which stems from the matched inflow profiles (Fig. 3) and the implementation of the Fitch WFP correction (Vollmer et al., 2024). This agreement indicates that turbine power is consistently modeled across both simulation frameworks, enabling a meaningful evaluation of model-specific biases. The MAV and MAVDX12D cases exhibit lower power due to the absence of an induction correction, while the DX2D and DX2DTKE100 cases slightly overestimate first-row power (Fig. 4b) as a result of marginally stronger inflow wind. Additionally, increasing the farm-added TKE enhances row-averaged power output by promoting more efficient wake recovery via momentum transport into the farm.

In the aligned LES, the power drops sharply in the second row (to ∼2 MW) and is followed by a gradual power recovery downstream (Figs. 4a,b), as is often observed in LES studies of dense offshore wind farms with an aligned layout (Allaerts and Meyers, 2017; Stevens and Meneveau, 2017; Stieren and Stevens, 2022; Stipa et al., 2024). For the staggered layout, the power decrease is smaller because the effective streamwise distance between turbine rows doubles compared to the aligned layout (Stieren and Stevens, 2022). None of the NWP-WFP simulations using Fitch capture the sharp drop in power, instead displaying a more gradual pattern of power decrease. The MAV and MAVDX12D cases (Fig. 4a) show agreement with the aligned LES due to a more accurate representation of subgrid wake effects, while only the DX2D and DX2DTKE100 cases

(Fig. 4b) achieve similar agreement through their finer spatial resolution ($\Delta X = 2D$). Coarser-resolution Fitch cases, regardless of the added TKE (Figs. 4a), tend to overestimate power in the upstream half of the farm when considering the aligned LES the reference. This power overestimation results from weaker wake losses, as the coarse NWP-WFP grid ($\Delta X = 1$ km) dilutes wake structures spatially. This limitation has been previously documented (Archer et al., 2020; Sanchez Gomez et al., 2024). The agreement improves considerably if the staggered LES case is considered the reference.

At finer resolution (cases DX2D and DX2DTKE100), wakes become sharper and induce more realistic power deficits in turbine rows 2–4 (Fig. 4b) compared with the aligned LES. The absence of power recovery beyond the second row in the NWP-WFP simulations, compared to the LES (Figs. 4a,b), likely stems from insufficient wake recovery, an aspect discussed further in Section 3.4.

In summary, the coarser NWP-WFP configurations, the Fitch WFP spatially averages the wind speed deficit over each grid cell, leading to an underestimation of wake losses at downstream turbines and a corresponding overestimation of power. This excess power implies enhanced momentum extraction within the wind farm, which modulates the wind speed at the farm exit. The MAV scheme mitigates this behavior by explicitly accounting for subgrid turbine-turbine wake interactions, resulting in more realistic wake losses and power levels. As a result, the wind speed at the wind farm exit, which is critical for downstream wake recovery, is more accurately represented when subgrid wake effects are included.

3.3 Wind farm wake flow field and spatial average

In this section, we compare the representations of hub-height wind speed and TKE by the LES and NWP-WFP simulations. The goal is to quantify the differences in wind farm wake structure and recovery between the aligned and staggered LES, spatially averaged to the grid of the BASE case (Fig. 5), and selected NWP-WFP cases (Fig. 6). The coarsened LES results for both aligned and staggered cases are obtained by spatially averaging the native-resolution LES data located within individual grid cells of the BASE case, enabling a direct comparison between the two (Figs. 5k–n), as in previous studies (Vanderwende et al., 2016; Peña et al., 2022; García-Santiago et al., 2024). The origin of the coordinate system is shifted to the southwest corner of the wind farm. Throughout the text, we divide the wind farm wake into three distinct regions: the intra-farm wake (0 km $< X <$ 11.2 km), the near-farm wake (11.2 km $< X <$ 15 km), and the far wake of the farm ($X >$ 15 km). The wind farm exit separates the intra-farm and near-farm wake regions. The thick black rectangle shows the wind farm perimeter as defined by the WFP. In the case DX2D (Fig. 6e,f), the finer resolution results in a smaller represented perimeter compared to the BASE case.

The full-resolution LES (Figs. 5a,b) exhibits sharp streaks of alternating low and high wind speed and TKE due to the aligned turbine layout (Stieren and Stevens, 2022; Stipa et al., 2024). These streaks extend approximately 3–5 km downstream before merging into a single and broader structure (Fig. 5a). For the staggered layout (Figs. 5e), the streaks are more broadly distributed in the spanwise direction. In contrast, the coarsened LES aggregates and smooths out these microscale variabilities (Fig. 5c,g), producing more homogeneous flow and turbulence fields within the farm. In the far wake region ($X >$ 15 km), the LES and coarsened LES fields become similar, as turbulent mixing has reduced the spatial gradients in wind speed and TKE.

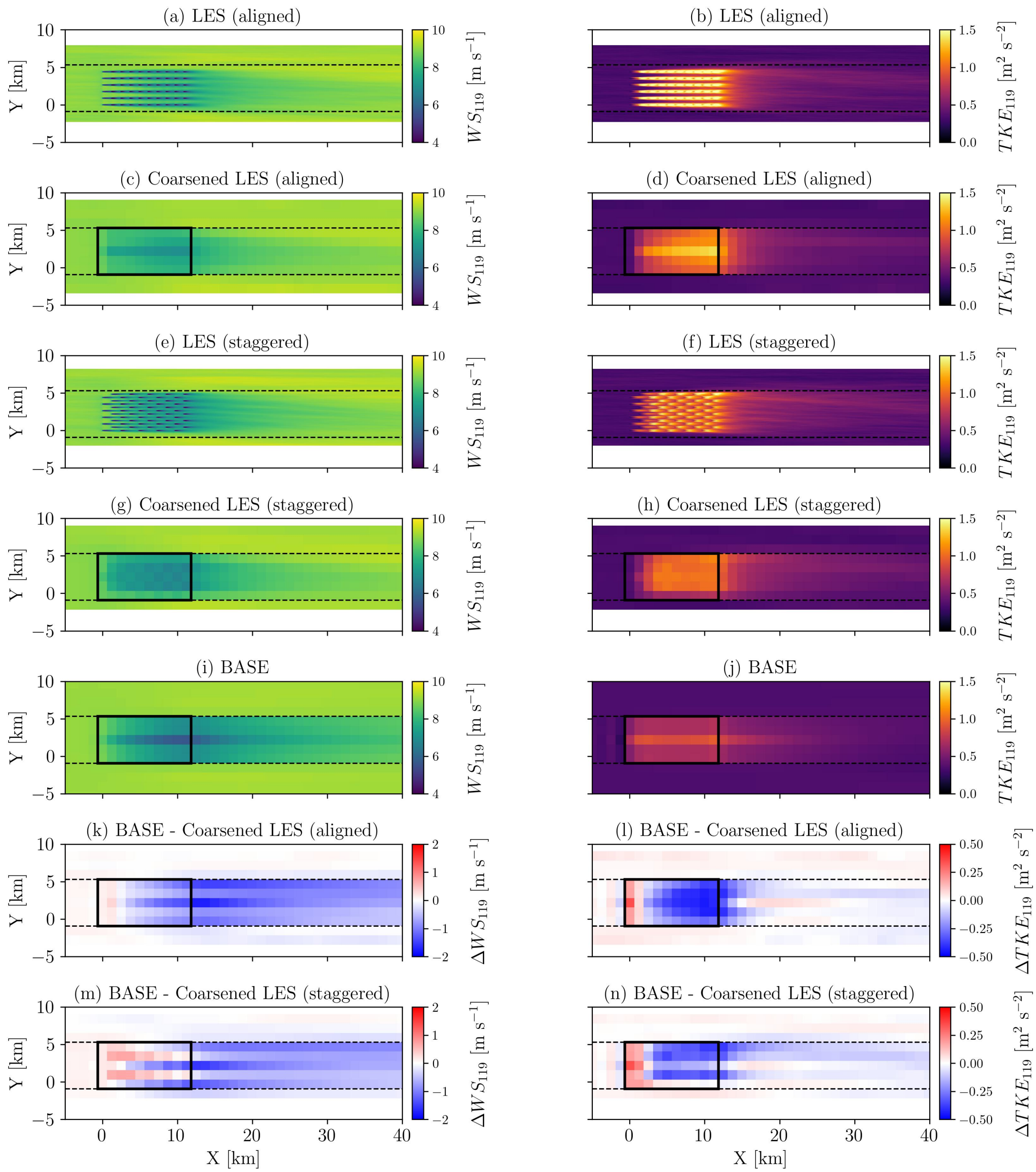

Figure 5. Time-averaged wind speed (WS_{119}) and TKE (TKE_{119}) at hub height for the aligned LES (a, b), coarsened aligned LES (c, d), staggered LES (e, f), coarsened staggered LES (g, h), NWP-WFP case BASE (i, j). The last two rows show the difference between the BASE case and the coarsened aligned (k, l) and staggered LES (m, n). The black rectangles indicate the wind farm perimeter as represented in the NWP-WFP simulation. Horizontal dashed lines mark the spanwise extent of the region used for averaging.

A persistent feature in the coarsened aligned LES, BASE and TKE100 cases (Figs. 5c,i and 6c) is a narrow band of reduced wind speed around $Y = 2.5$ km. This more intense wake results from the Y-direction turbine spacing ($s_y = 5D$) being finer

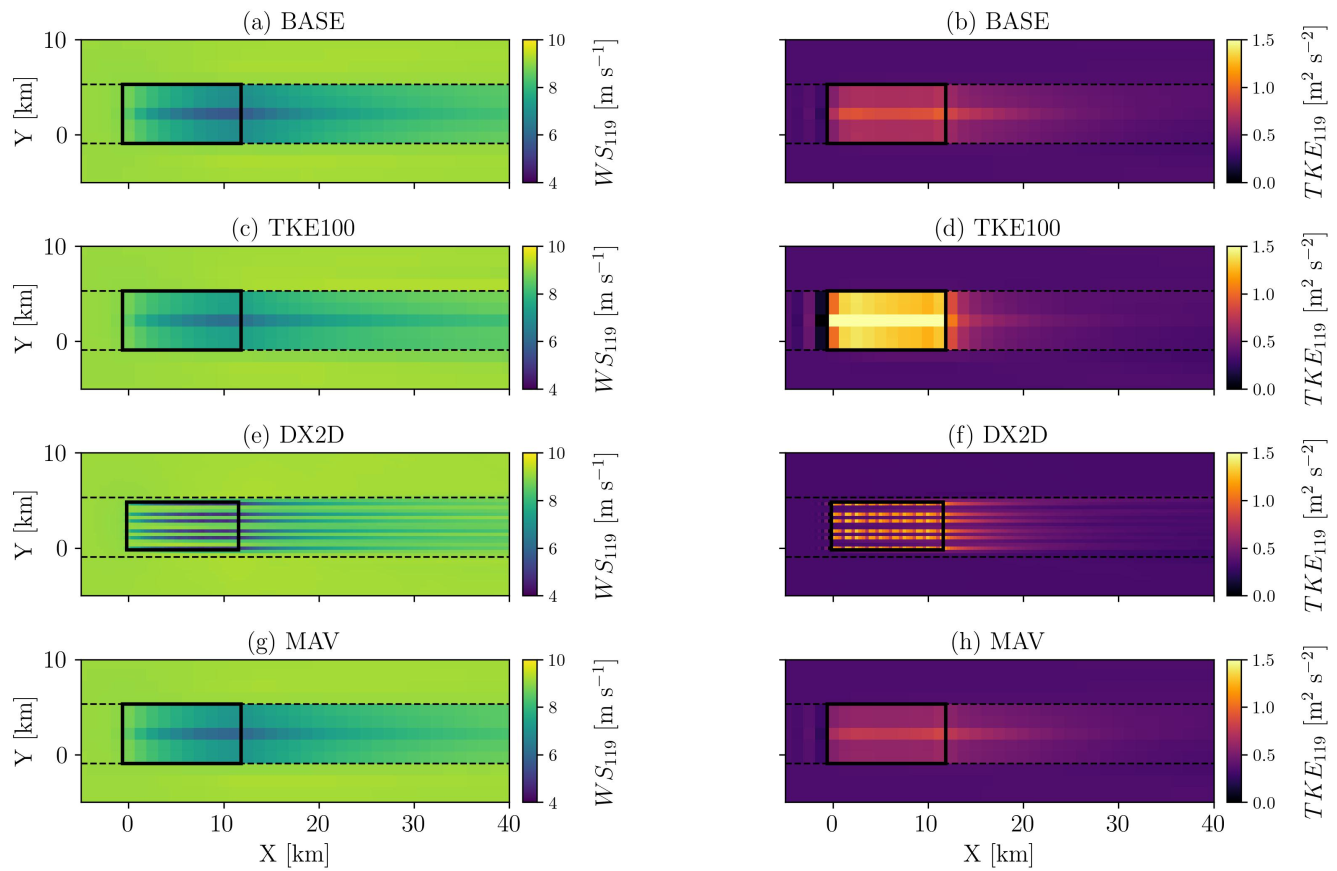

Figure 6. Time-averaged wind speed (WS_{119}) and TKE (TKE_{119}) at hub height for the NWP-WFP cases BASE (a, b), TKE100 (c, d) and DX2D (e, f) and MAV (g, h). The black rectangles indicate the wind farm perimeter as represented in the NWP-WFP simulation. Horizontal dashed lines mark the spanwise extent of the region used for averaging.

than the grid spacing ($\Delta X = 7D$), such that two turbine columns fall within a single grid cell. This aggregation produces a locally stronger momentum sink and TKE source (Fitch et al., 2012).

Although the total momentum sink in DX2D is comparable to BASE and TKE100, the local wind speed deficits are larger due to the finer resolution, which produces more concentrated wakes (Figs. 6e). This localization of the wind speed deficits explains the improved agreement with the aligned LES regarding the second-row power losses for cases DX2D and DX2DTKE100 (Fig. 4b).

The wind speed ($\Delta\, WS_{119}$) and TKE ($\Delta\, TKE_{119}$) differences, calculated as the BASE case minus the coarsened LES (Figs. 5k–n), are small upstream and beside the wind farm for both aligned and staggered layouts. Faint blue bands of negative $\Delta\, WS_{119}$ appear outside the spanwise averaging region, caused by stronger acceleration around the wind farm in the LES. Within the farm, $\Delta\, WS_{119}$ transitions from slightly positive in the first few rows, to near-zero at row 4, and then to negative further downstream. The strongest negative wind speed differences occur in the near-farm wake (11.2 km $< X <$ 15 km), followed by a modest recovery, but remain between -0.5 and -1 m s^{-1} in the far wake of the farm ($X >$ 20 km) for the aligned layout (Fig. 5k). For the staggered layout (Fig. 5m), wind speed differences are reduced, indicating improved agreement between the BASE case and the LES. For ΔTKE_{119}, the BASE case overestimates TKE compared to both the aligned and staggered LES in the first turbine row and underestimates it in rows 3 and further downstream. In the near-farm wake (11.2 km $< X <$ 15 km), the TKE remains underestimated but recovers further downstream ($X >$ 20 km) where the agreement with the LES is excellent.

3.4 Intra-farm, near-farm and far wake recovery

Here, we assess how the streamwise evolution of the wind farm wake is affected by changing the added TKE coefficient and WFP (Fig. 7) and the grid resolution (Fig. 8). The time-averaged wind speed and TKE are evaluated at hub height and averaged in the spanwise direction within the bounds ($Y = -0.923$ and 5.307 km) of the horizontal dashed lines represented in Fig. 5, the lateral extent of the wind farm in the reference BASE case. Furthermore, to mitigate averaging errors from the coarse mesoscale resolution near the spanwise boundaries, all results are first interpolated to a higher-resolution grid ($\Delta X = 50$ m).

In the intra-farm wake region, the momentum extraction by the turbines acts simultaneously with the wake recovery. The coarse Fitch simulations slightly underestimate the wind speed deficit in the first three turbine rows of the wind farm but overestimate the deficit further downstream (Figs. 7a) relative to the aligned LES. However, using the staggered LES as reference produces much better agreement in the second half of the wind farm, especially for the TKE050–100. Notably, the cases with α values of 75% and 100% show clear improvement at the wind farm exit and in the near-wake region ($X <$ 15 km) due to the enhanced momentum entrainment into the wake associated with the larger TKE.

The MAV cases are superior to Fitch's BASE case because the improved representation of subgrid wake effects leads to better turbine power and momentum extraction predictions (Ma et al., 2022a). Because of the smaller momentum extraction relative to the BASE case, the added TKE is also smaller. The similar trends in most variables (Figs. 7a–c) between the coarser MAVDX12D and the finer MAV demonstrate the consistency of this WFP across different spatial resolutions.

Simulations with the finest grid resolution (DX2D and DX2DTKE100) improve the representation of wind speed in the intra-farm and near-farm wake regions (Figs. 8a,d). This improvement is first attributed to the more realistic predictions of turbine power in these cases (Fig. 4b), which imply a more accurate extraction of momentum by the wind farm. As a result, the generated wake exhibits a wind speed deficit that more closely matches the aligned LES near the wind farm exit.

The combination of momentum extraction and wake recovery inside the wind farm creates the wind speed and TKE conditions at the farm exit (the red vertical dashed line in Fig. 7). This condition at the farm exit is relevant for the subsequent recovery of the near-farm wake. Among the cases varying the TKE coefficient (Fig. 7a), TKE100 most closely approximates the aligned LES at the farm exit. The agreement improves with the staggered LES as the reference. The TKE000 case is the worst performing because the momentum extraction is not counterbalanced by the wake recovery within the farm. The MAV cases perform better than Fitch's BASE case and would possibly perform even better with more added TKE considering the aligned LES.

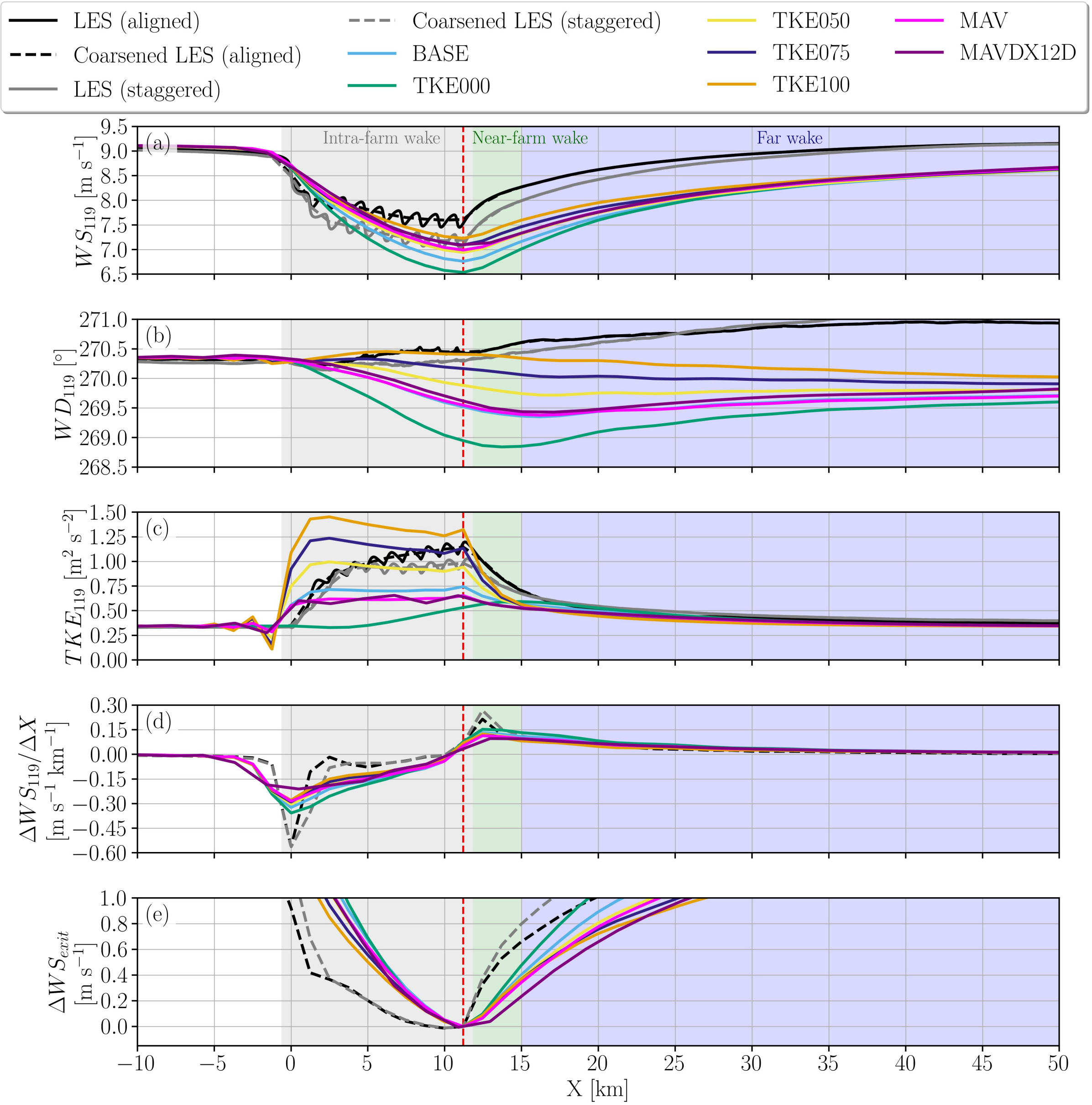

Figure 7. Streamwise variation of spanwise averages over the wind farm area of hub-height wind speed (a), wind direction (b), TKE (c), streamwise gradient of wind speed (d) and wind speed change relative to the wind farm exit (e) for the aligned and staggered LES at full resolution, coarsened LES, and NWP-WFP cases. The colored background areas indicate the streamwise extent of the intra-farm wake (gray), near-farm wake (green), and far wake of the farm (blue). The red vertical dashed line marks the wind farm exit.

The momentum extraction by the turbines ceases in the near-farm wake region so that the wake recovery rates can be evaluated in isolation. The streamwise gradient of wind speed ($\Delta WS_{119}/\Delta X$) and the wind speed change relative to the

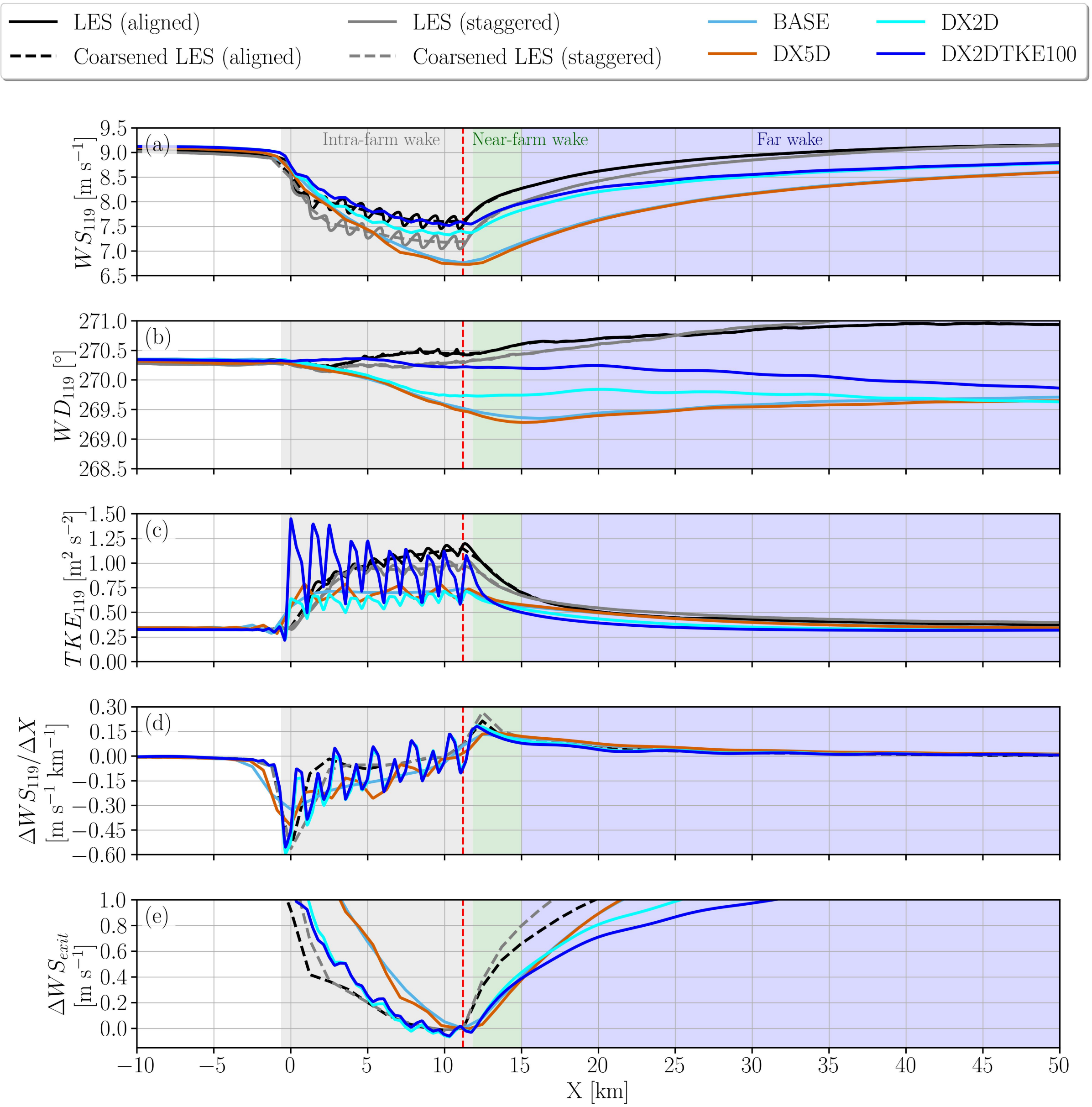

Figure 8. Same as Fig. 7, but for Fitch cases with different grid resolutions.

wind farm exit ($\Delta\, WS_{exit}$) quantify the near-farm wake recovery (Fig. 7d,e). The greatest divergence between the NWP-WFP simulations and the LES occurs in the near-farm wake ($11.2 < X < 15$ km), where the NWP-WFP simulations all fail to capture a peak in recovery rate (Fig. 7d). Thus, the wake recovery in the LES is faster immediately after the wind farm exit, which is also noticeable in the shape of the streamwise wind speed curvature (Fig. 7a). Even cases TKE100 and MAV, which most closely approximates the LES wind speed in the near-farm wake, underestimates the wake recovery rate downstream.

This discrepancy suggests that a key mechanism for wake recovery is not adequately captured in the NWP-WFP simulations in the near-farm wake.

The near-farm wake recovers slightly faster in finer-resolution cases, as evident in both the wind speed (Fig. 8a) and the streamwise gradients in wind speed (Fig. 8d), which now reproduce the peak displayed by the LES. Finally, adding more TKE ($\alpha = 100\%$) in the high-resolution simulation mostly influences the momentum extraction within the farm but has a weak influence on wake recovery rates.

Even though the difference in near-farm wake recovery rates between the NWP-WFP simulations and the LES occurs over a relatively short distance (∼1–2 km), it produces measurable bias in wind speeds. Notice that even if some cases match the wind speed (TKE100 and aligned LES) at the farm exit (Fig. 7a), a departure between the two curves occurs downstream. Between the wind farm exit at 11.2 km and 15 km, the gain in wind speed is of about 0.65 m s^{-1} and 0.8 m s^{-1} for the aligned and staggered LES (Fig. 7e), respectively. The change in wind speed is much smaller for the coarser resolution NWP-WFP cases, in the range between 0.2 and 0.5 m s^{-1} (Fig. 7e). On the other hand, the higher resolution cases gain about 0.4 m s^{-1} (Fig. 8e). Amongst the NWP-WFP simulations, case TKE000 displays the fastest near-farm wake recovery rate because of the largest wind speed deficit. Subtracting the wind speed change of the two LES with the NWP-WFP cases, a difference of 0.15–0.60 m s^{-1} is found. These values represent the bias in wind speed associated with the slower near-farm wake recovery in the NWP-WFP simulations.

None of the NWP-WFP simulations matches the wind speed of the LES in the far wake (Figs. 7a and 8a), but the wake recovery rates agree very well (Figs. 7d and 8d). The bias in wind speed decreases in the far wake for cases with strong deficit, such as BASE and TKE000. However, the bias remains mostly unchanged for cases with weaker deficit at the farm exit, such as TKE100, DX2D and DX2DTKE100. Overall, regardless of the TKE coefficient, all the mesoscale simulations display a consistent negative wind speed bias ranging from approximately -0.7 m s^{-1} (TKE000) to -1.3 m s^{-1} (TKE100) in the near-farm wake at $X = 15$ km. The bias decreases to approximately -0.6 m s^{-1} in the far wake ($X = 50$ km) for all cases (Fig. 7a) compared to the LES.

In the LES, TKE builds up gradually, row by row, whereas in the NWP-WFP cases with a TKE source ($\alpha > 0$), the TKE peaks near the first few turbine rows and then decreases monotonically downstream (Fig. 7c). The TKE remains nearly constant within the farm in case BASE, and is small throughout in case TKE000, which lacks an explicit TKE source. Interestingly, cases with α of 25% and 50% better match the TKE levels near the first turbine rows, consistent with results from Archer et al. (2020), while those with higher α (75%, 100%) better match the TKE in the latter half of the farm, in line with other findings (Larsén and Fischereit, 2021; Ali et al., 2023). This variability in the literature seems to stem in part from where the comparison is made: within, near or further downstream of the wind farm, as shown here.

A key insight is that turbine-added TKE does not evolve properly within the wind farm in the NWP-WFP simulations, even when its magnitude matches or exceeds that of the LES in the first few turbine rows. The root problem therefore lies not only in the amount of turbine-added TKE, as a gradual reduction of intra-farm TKE persists across several cases (TKE050–TKE100). Moreover, TKE decreases more rapidly than in the LES in the near-farm wake (Fig. 7c). While this behavior in the NWP-WFP simulations could in principle be attributed to excessive dissipation, Section 4.1.2 provides additional evidence that insufficient shear production of TKE, rather than dissipation, plays the dominant role.

Lastly, the underestimation of the subtle anti-clockwise turning of the wake depends on turbulent mixing (Fig. 7b). For the wake turning, this behavior results from downward turbulent momentum entrainment, which transports more veered wind from aloft into the wake (van der Laan and Sørensen, 2017; Gadde and Stevens, 2019; Englberger et al., 2020; Stieren et al., 2022; Kasper et al., 2024). Accordingly, cases with weaker entrainment, such as TKE000 and BASE, show a stronger directional bias. Although the absolute differences in wind direction are small (about 1° between TKE000 and TKE100), over long distances these differences may accumulate into downstream power losses for adjacent wind farms.

3.5 Under-resolved spatial gradients in the NWP-WFP simulation wake

In this section, we examine spatial gradients in the wind farm wake as represented by the aligned LES at full resolution and when spatially averaged to match the grid resolution of the BASE case. We also compare the LES results with the NWP-WFP cases BASE and TKE100. The goal is to evaluate how the realistic spatial gradients of the LES influence wake recovery, and how the horizontal and vertical gradients of the latter compare with the NWP-WFP simulations. Figures 9 and 10 intentionally focus on localized profiles at specific turbine-aligned grid cells to highlight differences in resolved gradients between the NWP-WFP simulations and the LES. While spanwise averaging would yield different absolute TKE levels, such averaging would obscure the local shear and turbulence structures that directly control wake recovery in the near-farm region. These figures are therefore not intended to represent farm-averaged behavior, but rather to diagnose the structural deficiencies of mesoscale simulations at the grid-cell scale.

The discrepancy between the coarsened aligned LES and the BASE and TKE100 wind speed profiles increases with downstream distance. The stronger momentum extraction in the staggered LES, relative to the aligned LES, results in improved agreement with the BASE and TKE100 cases. Figure 9 shows hub-height profiles of wind speed (Figs. 9a–e) and TKE (Figs. 9f–j) along the spanwise (Y) direction at selected streamwise distances: the wind farm entrance ($X = 0$ km), middle ($X = 5$ km), exit ($X = 11.2$ km), and two downstream locations ($X = 15$ and 20 km). At the entrance ($X = 0$ km), the spatially averaged LES gradients in wind speed (both coarsened LES) agree reasonably well with both NWP-WFP cases (Figs. 9a). However, deviations become noticeable at $X = 5$ km (Figs. 9b), especially between the coarsened aligned LES and the BASE case, and grow progressively larger through $X = 11.2$ and 15 km (Figs. 9c and d). At $X = 20$ km (Figs. 9e), the discrepancy remains large. The narrow band of reduced wind speed and increased TKE near the center of the wind farm in the Y direction is created by the existence of two turbines within that grid cell (Fig. 2b), as discussed in Section 3.3.

From the standpoint of spatial wind speed gradients, differences between both the aligned and staggered layout LES and the NWP-WFP cases are striking. While the coarsened LES profile appears similar to those of the NWP-WFP cases within the wind farm ($0 \leq X \leq 11.2$ km, $0 \leq X/D \leq 63$), this similarity hides strong localized gradients in the wakes that only appear in the non-averaged LES (Figs.9a–c). These strong localized gradients are expected with a fine-resolution grid and facilitate faster wake recovery in the LES. Notably, model discrepancies in wind speed profiles grow with streamwise distance while these strong localized gradients persist ($0 \leq X \leq 11.2$ km, $0 \leq X/D \leq 63$), but no longer increase between $X = 15$ and

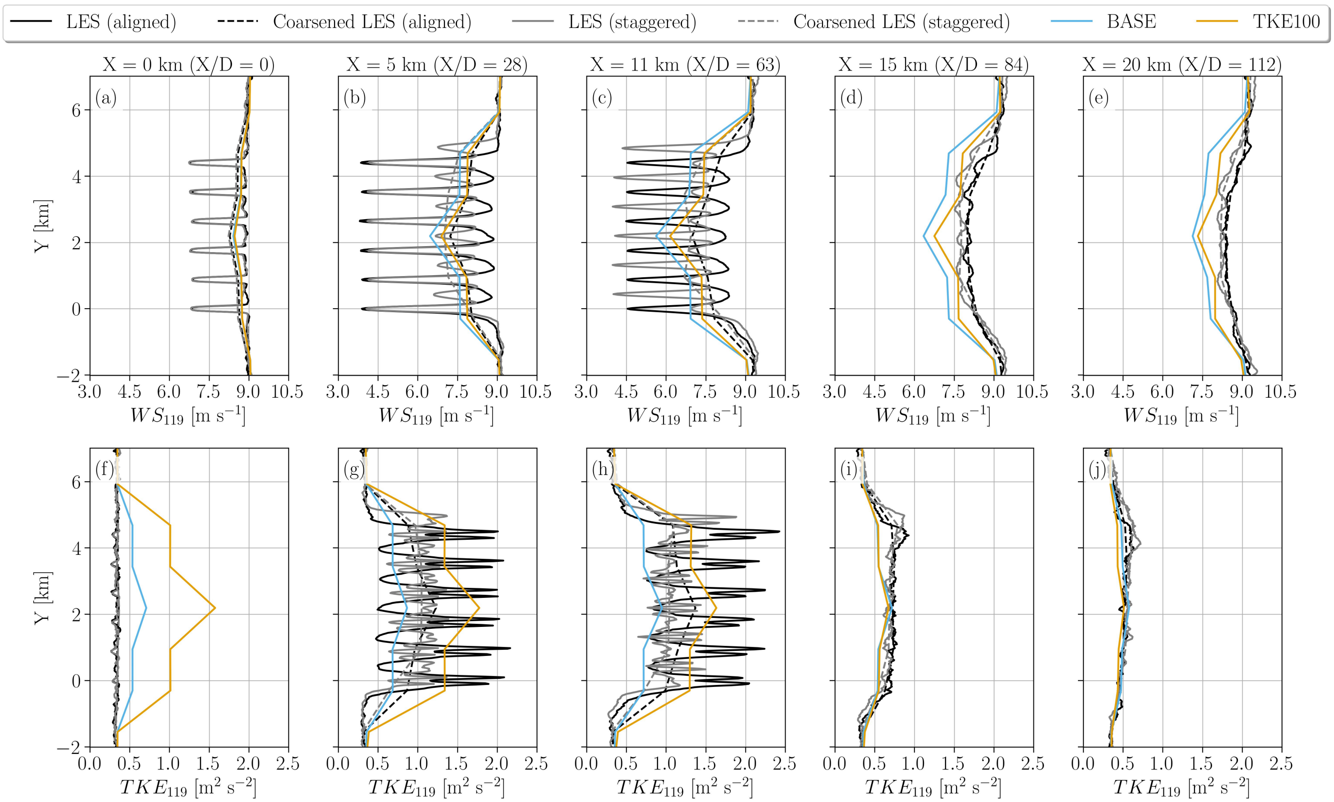

Figure 9. Time-averaged wind speed (a–e) and TKE (f–j) at hub height (119 m AGL) along spanwise Y lines at specific streamwise distances X (expressed as X/D in parentheses) for the aligned and staggered layout LES, coarsened LES, and NWP-WFP BASE and TKE100 cases.

20 km ($X/D = 84$ and 112, respectively), where the LES gradients become smoother and more comparable to those in the NWP-WFP cases.

This behavior suggests that the fundamental problem lies upstream, within the intra-farm and near-farm wake regions. Once the strong localized gradients in the wakes disappear in the LES, the differences between models stabilize. Therefore, the persistent lower wind speeds in NWP-WFP simulations in the far wake of the farm (Figs. 9d,e) are not caused by conditions there, but rather reflect limitations in representing spatial gradients and turbulent mixing within the intra-farm and near-farm wake regions. As conceptually illustrated in the Introduction, the slow wake recovery (Figs. 1b,c) and TKE decrease (Figs. 1e,f) are evident in the results shown in Figs. 9c,d and h,i, respectively.

Vertical profiles reveal how wind farm effects modify wind speed (Figs. 10a–f) and TKE (Figs. 10g–l) gradients in each simulation. Vertical profiles are sampled along the southernmost turbine column (near $Y = 0$ km) at selected streamwise locations to examine how each simulation resolves local vertical gradients. The data are not spatially averaged, allowing direct assessment of the gradients resolved by each grid. Upstream of the farm, wind speed (Fig. 10a) and TKE (Fig. 10g) profiles are nearly identical across simulations. Within and downstream of the farm, momentum extraction (Figs. 10b–d) and TKE production (Figs. 10h–j) alter these profiles. In the LES, the stronger wind speed deficit enhances vertical shear, especially near the rotor top tip, by $X/D = 28$ (Figs. 10b–d), leading to intense TKE generation in the same region (Figs. 10i–j). Combined, the stronger vertical wind speed gradient and enhanced TKE in the LES contribute to a faster intra-farm and near-farm wake recovery.

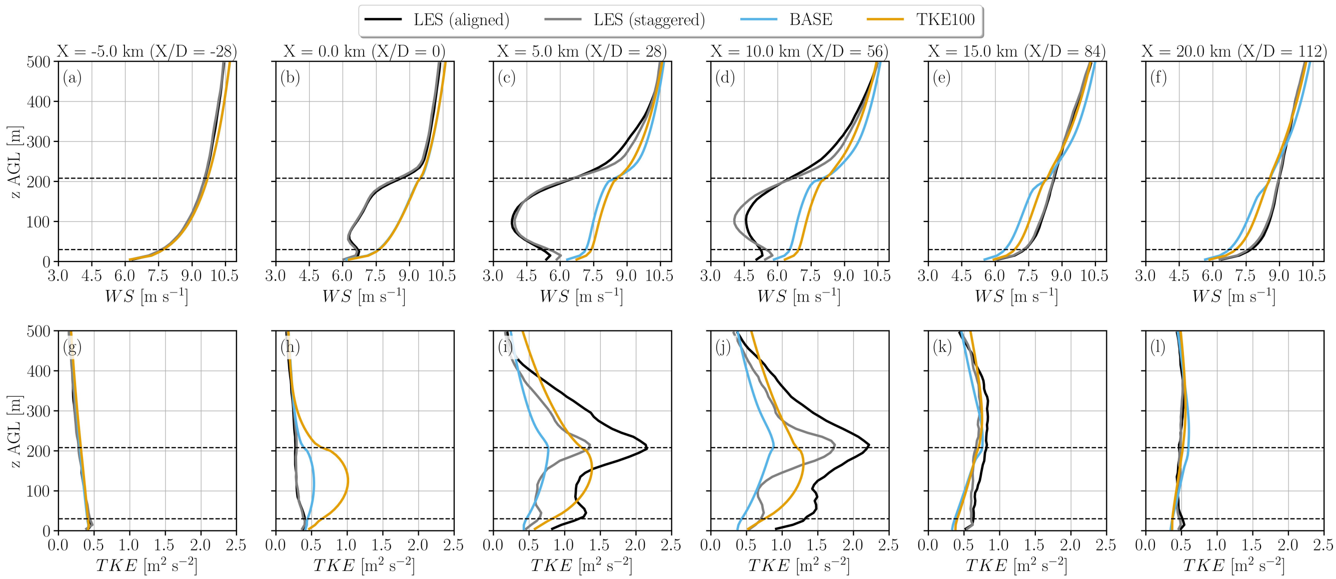

Figure 10. Vertical profiles of time-averaged wind speed (a–f) and TKE (g–l) at specific streamwise distances X (expressed as X/D in parentheses) probed over the southernmost column of turbines near $Y = 0$ km. The aligned and staggered layout LES without spatial averaging and NWP-WFP cases BASE and TKE100 are shown. The dashed horizontal lines represent the rotor top and bottom tips.

Despite the fine vertical resolution, NWP-WFP simulations fail to capture strong vertical gradients due to coarse horizontal resolution. Although the NWP-WFP simulations use the same vertical resolution as the LES ($\Delta z \sim 10$ m), they locally under-resolve vertical wind speed gradients (Figs. 10b–d). Both the LES show a much sharper local wind speed deficit (Figs. 10b–d), while in the NWP-WFP simulations the deficit is diluted due to spatial averaging over the coarser horizontal grid ($\Delta X \sim 1$ km). This horizontal averaging dilutes the momentum sink effect, weakening both horizontal and vertical gradients. As a result, even with sufficient vertical resolution, the vertical structure of the wake is poorly captured in the NWP-WFP simulations due to the coupling between horizontal and vertical gradients.

Further evidence of the critical role of under-resolved gradients in intra-farm and near-farm wake recovery emerges when evaluating the effect of TKE. From a turbulent mixing perspective, increased TKE accelerates wake recovery: for instance, the TKE100 case displays faster recovery than the BASE case, as also shown by Rosencrans et al. (2024). However, despite exhibiting more TKE than both the coarsened LES throughout much of the wind farm ($0 \leq X \leq 11.2$ km), including earlier onset of added TKE (Fig. 9f), the TKE100 wake still recovers slower than that of the LES. These findings highlight that enhanced farm-added TKE alone is insufficient to compensate for the under-resolved gradients.

4 Discussion

4.1 What are the fundamental problems?

The preceding results identify two interconnected sources of modeling bias: (i) under-resolved spatial gradients in turbine wakes and (ii) low TKE behind wind farms in NWP-WFP simulations. *Under-resolved*, rather than *unresolved*, is appropriate since the mesoscale grid partially captures the turbine-induced wind speed gradients, but lacks sufficient fidelity. These two issues affect the physics of wake recovery, which is governed by two interrelated mechanisms:

(a) the magnitude of turbulent mixing, and

(b) the strength of spatial gradients in the mean wind velocity field.

The recovery of momentum in wind turbine and near-farm wakes occurs through lateral and vertical turbulent entrainment of momentum, expressed as divergences of $\overline{u'v'}$ and $\overline{u'w'}$, respectively (Vermeer et al., 2003; Cal et al., 2010; Calaf et al., 2010; Abkar and Porté-Agel, 2015; Porté-Agel et al., 2020; Stieren and Stevens, 2022; van der Laan et al., 2023). Here, u', v', and w' denote fluctuations relative to the time-averaged wind velocity components U, V, and W in the streamwise, spanwise, and vertical directions, respectively. These momentum fluxes are commonly approximated using the Boussinesq hypothesis (Boussinesq, 1897; van der Laan et al., 2023) or equivalently the K-theory (Stull, 1988):

$$\overline{u'v'} = K_m \frac{\partial U}{\partial y} \tag{1}$$

$$\overline{u'w'} = K_m \frac{\partial U}{\partial z}. \tag{2}$$

Here, K_m is the eddy viscosity, which depends on turbulence and atmospheric stability (Stull, 1988), and $\frac{\partial U}{\partial y}$ and $\frac{\partial U}{\partial z}$ are the spanwise and vertical gradients of wind speed (for convenience, we assume the mean flow aligns with the x-direction). The eddy viscosity K_m increases with TKE, and therefore wakes tend to recover more rapidly under convective conditions compared to neutral or stable conditions (Magnusson and Smedman, 1994; Iungo et al., 2013; Fitch et al., 2013a; Mirocha et al., 2015; Abkar and Porté-Agel, 2015; Stevens and Meneveau, 2017; Bodini et al., 2017; Lundquist et al., 2019; Rosencrans et al., 2024; García-Santiago et al., 2024). The two modeling biases identified above directly impact these physical mechanisms of wake recovery:

(i) Under-resolved spatial gradients: weaken the mean shear in the wake, thereby reducing the turbulent fluxes [affecting factor (b)]. Even if TKE is present, the lack of strong horizontal and vertical gradients limits momentum transport into the wake.

(ii) Low TKE: reduces the eddy viscosity K_m, which diminishes the efficiency of turbulent mixing [affecting factor (a)]. As a result, the momentum recovery by turbulence is suppressed, even in regions where spatial gradients are better resolved.

In the following subsections, we examine each of these two problems in more detail. We begin with the role of under-resolved wind speed gradients and their consequences for wake recovery, followed by the impact of artificially low TKE in the farm region.

4.1.1 Under-resolved wind speed gradients

The first and perhaps most critical problem is that NWP-WFP simulations cannot accurately represent the spatial wind speed gradients that drive intra-farm and near-farm wake recovery. Many studies have shown that WFPs can reproduce wind speed deficits at turbine grid cells that generally resemble those from LES (Vanderwende et al., 2016; Abkar and Porté-Agel, 2015; Archer et al., 2020; Peña et al., 2022; García-Santiago et al., 2024). However, a closer look at the downstream regions reveals a slower wake recovery in NWP-WFP simulations compared to LES (e.g., Figs. 4a,c in Vanderwende et al. (2016); Fig. 7 in Archer et al. (2020); Figs. 11–13 in Peña et al. (2022); Figs. 4 and 7 in García-Santiago et al. (2024)). Here, we demonstrate that this discrepancy arises because the momentum sink term in WFPs is not resolved by the grid, and thus is not severely affected by its coarseness, whereas the wake recovery is fundamentally resolved by the grid. Specifically, the NWP-WFP simulations exhibit inherently weaker horizontal (Figs. 9a–c) and vertical (Figs. 10b–d) gradients in the wind velocity field within the intra-farm and near-farm wake regions, i.e. $\frac{\partial U}{\partial y}|_{\mathrm{NWP-WFP}} << \frac{\partial U}{\partial y}|_{\mathrm{LES}}$ and $\frac{\partial U}{\partial z}|_{\mathrm{NWP-WFP}} << \frac{\partial U}{\partial z}|_{\mathrm{LES}}$, respectively. While discrete velocity differences evaluated at WRF grid resolution can locally yield gradients comparable to or even exceeding those in a coarsened LES (Fig. 9d), they do not organize into shear structures comparable to those present in the native-resolution LES. In contrast, the LES at native resolution exhibits spatially coherent and persistent shear layers that extend downstream and continuously drive turbulence production and wake recovery, a structural feature that is not maintained in the mesoscale representation.

As a result, even when farm-added TKE levels are comparable to or exceed those in the LES, the intra-farm and near-farm wake recovery (driven by the weaker gradients) remains underestimated in the NWP-WFP simulations (Sections 3.4 and 3.5). The fact that simulations with the finest grid resolution (DX2D and DX2DTKE100), which better resolve spatial gradients, improve the representation of the near-farm wake recovery (Figs. 8a,d) supports this argument. Under-resolved gradients have also been noticed by others (Fischereit et al., 2022b). Related, in another study using WRF and the Fitch WFP (Pryor et al., 2020), shorter wind farm wakes result from finer grid resolutions, which could in part be explained by the impact of the under-resolved gradients on wake recovery.

4.1.2 Insufficient shear production causes low TKE

The second problem is the relatively fast decrease of farm-added TKE in the NWP-WFP simulations compared to the LES. This comparatively low TKE in the near-farm wake reduces turbulent mixing, effectively lowering the eddy viscosity K_m, and further slowing wake recovery. Even when large amounts of turbine-added TKE are injected (e.g., $\alpha = 75\%$ or 100%), the TKE fails to accumulate row-by-row as it does in the LES (Fig. 7c). Across all tested TKE enhancement levels ($\alpha = 25\%$–100%), the NWP-WFP TKE returns to near-ambient levels within 5 km downstream, almost twice as fast as in the LES.

A compelling hypothesis is that the rapid reduction of TKE is not merely a dissipation artifact, but instead a consequence of under-resolved gradients. This interpretation is supported by the close agreement between NWP-WFP and LES TKE levels in the inflow (Fig. 3d) and in the far wake (Fig. 7c), indicating that the mesoscale model does not inherently over-dissipate TKE. Rather, the limitation emerges in the intra- and near-farm wake, where TKE is insufficiently generated because shear production depends on spatial gradients (Mellor and Yamada, 1982; Nakanishi and Niino, 2009) that are under-resolved at mesoscale resolution. The coupling between TKE, shear production, and dissipation is illustrated in Appendix B. While this limitation can be partially offset within the wind farm through turbine-added TKE, it becomes evident downstream, where the WFP is inactive and TKE levels fall below those of the LES. This mechanism is therefore intrinsic to NWP-WFP frameworks and has implications for studies that focus on modifying turbine-added TKE formulations (Fitch et al., 2012; Archer et al., 2020; Khanjari et al., 2025).

4.2 Implications

Because both problems – slow wake recovery and insufficient shear production of TKE – are fundamentally linked to grid resolution, they are likely to affect wake recovery not only in WRF with the Fitch or MAV WFPs but also in other NWP and climate models that use WFPs. As such, these findings underscore the need for improved representation of both spatial gradients and turbulent mixing if WFPs are to accurately simulate wind farm wakes and their downstream impacts. Building on this, we present implications of our work for studies of real wind farm wake effects, where environmental and observational aspects increase the complexity of the analysis. We highlight the importance of separating wake generation (momentum extraction) from its recovery when evaluating model performance.

Some NWP-WFP simulations driven by realistic synoptic conditions have demonstrated reasonable agreement with observed wind speed deficits in wind farm wakes, based on aircraft measurements (Siedersleben et al., 2018a, b, 2020; Larsén and Fischereit, 2021; Ali et al., 2023; van Stratum et al., 2022) and SCADA data (Sanchez Gomez et al., 2024) from offshore sites. However, discrepancies in inflow conditions between simulations and observations remain a major challenge, as they can obscure the evaluation of wake recovery. Despite this, several case studies have achieved good correspondence with observed wind speed profiles along wind farm transects. Given the inherent spatio-temporal variability and limited control over inflow in realistic configurations, such results are promising. In contrast, our idealized setup ensures excellent agreement in the inflow, allowing a more direct assessment of WFP performance and limitations. These controlled conditions provide valuable guidance for improving their representation in more complex, operational scenarios.

Another important issue is the separation between wake generation and recovery for modeling evaluation. The wind speed bias between the NWP-WFP simulation and the LES within the wind farm in not exclusively caused by a difference in wake recovery, but also by a difference in momentum extraction. For instance, in Fig. 4b, the coarser-resolution cases BASE and DX5D have larger row-averaged power (extract more momentum) than the finer-resolution cases DX2D and DX2DTKE100. As a result, in combination with differences in wake recovery between the simulations, cases BASE and DX5D have stronger wind speed deficits (Fig. 8a). Matching the wind speed deficit predicted by LES or observations does not necessarily mean the dynamics of wake recovery are well represented in NWP-WFP simulations. For instance, a seemingly faster wake recovery was attributed to the NWP-WFP simulation in comparison with the LES, when in fact the NWP-WFP simulation generated a much weaker wake in the first place (Eriksson et al., 2015). As the stronger wake of the LES recovers momentum, it eventually matches the wind speed deficit of the weaker wake of the NWP-WFP simulation downstream. Thus, wake generation and recovery are two important aspects of wind farm flows that need to be considered simultaneously.

The degree of wake recovery underestimation is likely sensitive to inflow wind speed, direction and atmospheric stability. For instance, the weaker ambient turbulence in stable conditions promotes longer individual turbine wakes (and thus stronger spatial gradients in wind speed) in comparison with neutral or convective conditions (Abkar and Porté-Agel, 2015; Abkar et al., 2016b). Hypothetically, these unmixed wind speed gradients could further slow wake recovery in NWP-WFP simulations, which requires more research. Evaluating wake recovery in stable conditions is important because it is exactly when wakes are most pronounced (Magnusson and Smedman, 1994; Iungo et al., 2013; Fitch et al., 2013a; Mirocha et al., 2015; Abkar and Porté-Agel, 2015; Bodini et al., 2017; Lundquist et al., 2019; Rosencrans et al., 2024; García-Santiago et al., 2024).

5 Conclusions

Numerical Weather Prediction (NWP) and climate models equipped with Wind Farm Parameterizations (WFPs) provide a powerful framework for simulating wind farm cluster wakes, both onshore and offshore. Their ability to capture physical processes across a wide range of spatiotemporal scales enables studies of atmosphere–wind farm interactions under realistic conditions and over large computational domains. In this paper, we assess the strengths and limitations of the NWP-WFP approach using the Weather Research and Forecasting (WRF) model with the Fitch et al. (2012) and MAV (Ma et al., 2022b, a) WFPs, in comparison to the neutrally-stratified large-eddy simulation (LES) of Kasper et al. (2024). We find that near-farm wake recovery is slower in the NWP-WFP simulations relative to the LES for two interconnected reasons: (i) under-resolved spatial gradients in the wind velocity field and (ii) insufficient shear production of turbulence kinetic energy (TKE).

The first issue stems from the fact that in the LES, near-farm wake recovery is driven by sharp local velocity gradients and enhanced turbulent mixing that replenishes momentum in the wake. In contrast, while the NWP-WFP momentum deficit at the turbine grid cell is *unresolved* by the grid, its downstream recovery depends on grid-resolved gradients. However, these horizontal and vertical gradients in wind speed in the intra- and near-farm wake are *under-resolved* at the mesoscale grid spacing used in NWP-WFP, leading to underestimated wake recovery.

In the near-farm wake, differences in wind speed recovery between the NWP-WFP simulations and the LES emerge over a short downstream distance ($\sim$1–2km) but lead to measurable wind speed biases. Between the wind-farm exit at 11.2 km and 15 km downstream, the LES recovers approximately 0.65–0.8 m s^{-1}, whereas the coarser-resolution NWP-WFP simulations recovers only 0.2–0.5 s^{-1}, yielding a wind speed bias of about 0.15–0.60 m s^{-1}. Higher-resolution mesoscale simulations reduce this bias, with wind-speed increases of roughly 0.4 m s^{-1}, but differences relative to the LES remain. Despite similarly fine vertical grid spacing, horizontal smearing of the momentum deficit in the NWP-WFP simulations leads to under-represented horizontal and vertical gradients. Even simulations with increased turbine-added TKE cannot fully compensate for these limitations, indicating that under-resolved gradients constrain wake recovery behind the wind farm.

The second issue involves the insufficient shear production of TKE. In the LES, TKE increases progressively along the wind farm rows, peaking near the wind farm exit. In the NWP-WFP simulations, however, the maximum occurs within the first few rows and then decreases monotonically along the streamwise direction. Most importantly, the TKE decreases faster than in the LES in the near-farm wake region (within 4 km downstream), likely due to the same insufficient shear production. The inflow profiles have similar shear and veer characteristics across simulations, which initially produce comparable TKE levels. However, the insufficient magnitude of spatial gradients in the intra- and near-farm wake in the NWP-WFP undermines the local shear production of TKE. As a result, the TKE returns to ambient levels much faster than in the LES and further undermines wake recovery in these neutrally-stratified simulations.

A key insight is that the slow recovery in the near-farm wake, although confined to a short downstream distance, has lasting consequences for the far wake region. In coarse-resolution simulations, the far wake wind speed bias remains substantial even when large amounts of turbine-added TKE are introduced. However, when near-farm wake recovery improves through finer grid resolution and better-resolved gradients, the far wake bias is also reduced. Thus, accurately representing near-farm wake recovery is also essential for reducing modeling biases in the far wake downstream.

Because these two findings stem from the relatively coarse mesoscale grid, they are relevant to other NWP and climate modeling frameworks that employ any form of WFP. We note that the slower wake recovery compared with the LES arises from the coarse representation of wake recovery processes at the mesoscale, rather than from deficiencies in the WFPs themselves. This slower wake recovery occurs predominantly in the near-farm wake, a region that lies outside the direct influence of the WFPs and is therefore governed by grid-resolved dynamics and planetary boundary layer (PBL) schemes. Naturally, the WFPs exert influence on wake recovery since they affect wind speed and TKE at the wind farm exit. Therefore, beyond improving the subgrid parameterizations of momentum sinks and TKE sources, it is equally important to develop new strategies that account for the effects of under-resolved gradients, especially in the near-farm wake. These efforts should produce spatial variations of TKE and wake recovery rates more consistent with LES. A potential pathway forward is the development of a subgrid model that accounts for the missing spatial gradients driving wake recovery. Such a model would act over grid cells downstream of the wind farm in the near-farm wake and be evaluated against LES, potentially using empirical tuning. Otherwise, the underestimation of wake recovery may lead to overestimated wake losses.

Future work could: (i) propose methods to address the problem of under-resolved gradients and (ii) assess wake recovery under varying atmospheric stability regimes. Another possible direction is to (iii) investigate whether different planetary boundary layer (PBL) schemes can improve turbulent mixing and thus wake recovery, such as the 3DPBL scheme (Kosović et al., 2020; Juliano et al., 2022). Regarding (ii), we note that the velocity gradients in the LES become smoother and more mesoscale-resolvable beyond approximately 5 km downstream. Under such conditions, NWP-WFP simulations may better reproduce the reference LES recovery. Following this rationale, convective boundary layers, by mixing sharp gradients more efficiently, may allow NWP-WFP to more accurately capture wake recovery than is possible under neutral or stable conditions. Therefore, understanding the role of atmospheric stability on wake recovery is also necessary for improving the accuracy of NWP-WFP approaches.

Code and data availability. The WRF model version 4.4 with the axial induction correction (Vollmer et al., 2024) and the MAV WFP (Ma et al., 2022b, a) is available at https://github.com/wradunz/WRFv4.4-DRM_GAD.git. The WRF setup files for the NWP-WFP simulations can be accessed at Radünz (2025).

Appendix A: DTU 10-MW turbine power and thrust curves

This section evaluates the sensitivity of wake recovery to the thrust coefficient (C_T), as outlined in Table 1. The power and thrust coefficient curves for the DTU 10-MW wind turbine are shown in Figs. A1a,b, respectively. For an inflow wind speed of approximately 9 m s^{-1}, the turbine produces slightly over 5 MW of power, and the corresponding C_T is approximately 0.81.

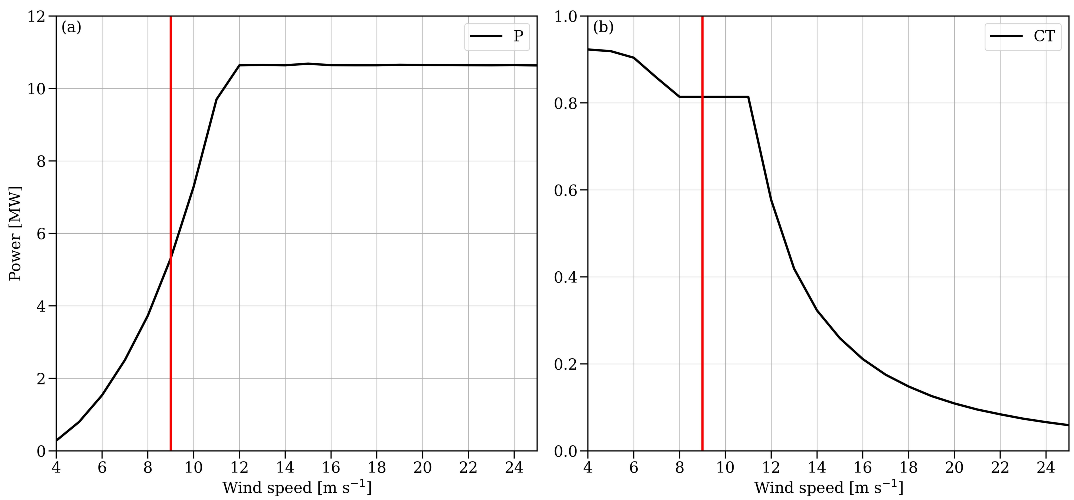

Figure A1. Power (a) and thrust coefficient (b) curves as function of wind speed for the wind turbine of the DTU 10-MW model. The red vertical line denotes the point of operation based on the hub height wind speed of approximately 9 m s^{-1} considered in this study.

The value of $C_T = 0.75$ adopted in the LES (Section 2.1) yields wind speed deficits similar to those obtained with a fixed C_T of 0.81 or with a wind-speed-dependent C_T (Fig. A2a). In contrast, using a lower C_T value of 0.50 results in a weaker wake and reduced TKE generation (Fig. A2c), since the TKE source term is proportional to the difference $C_T - C_P$. Therefore, whether C_T is set to 0.81, 0.75, or dynamically determined based on wind speed, the main conclusions of our investigation remain unchanged.

Appendix B: Streamwise TKE budget in NWP-WFP simulations

To support the interpretation presented in Section 4.1, we examine the streamwise evolution of selected MYNN TKE budget terms at hub height for the mesoscale NWP-WFP simulations (BASE, TKE100, and MAV), shown in Fig. B1. The budget terms are computed using the same spanwise averaging applied in Figs. 7 and 8, ensuring consistency with the bulk wake

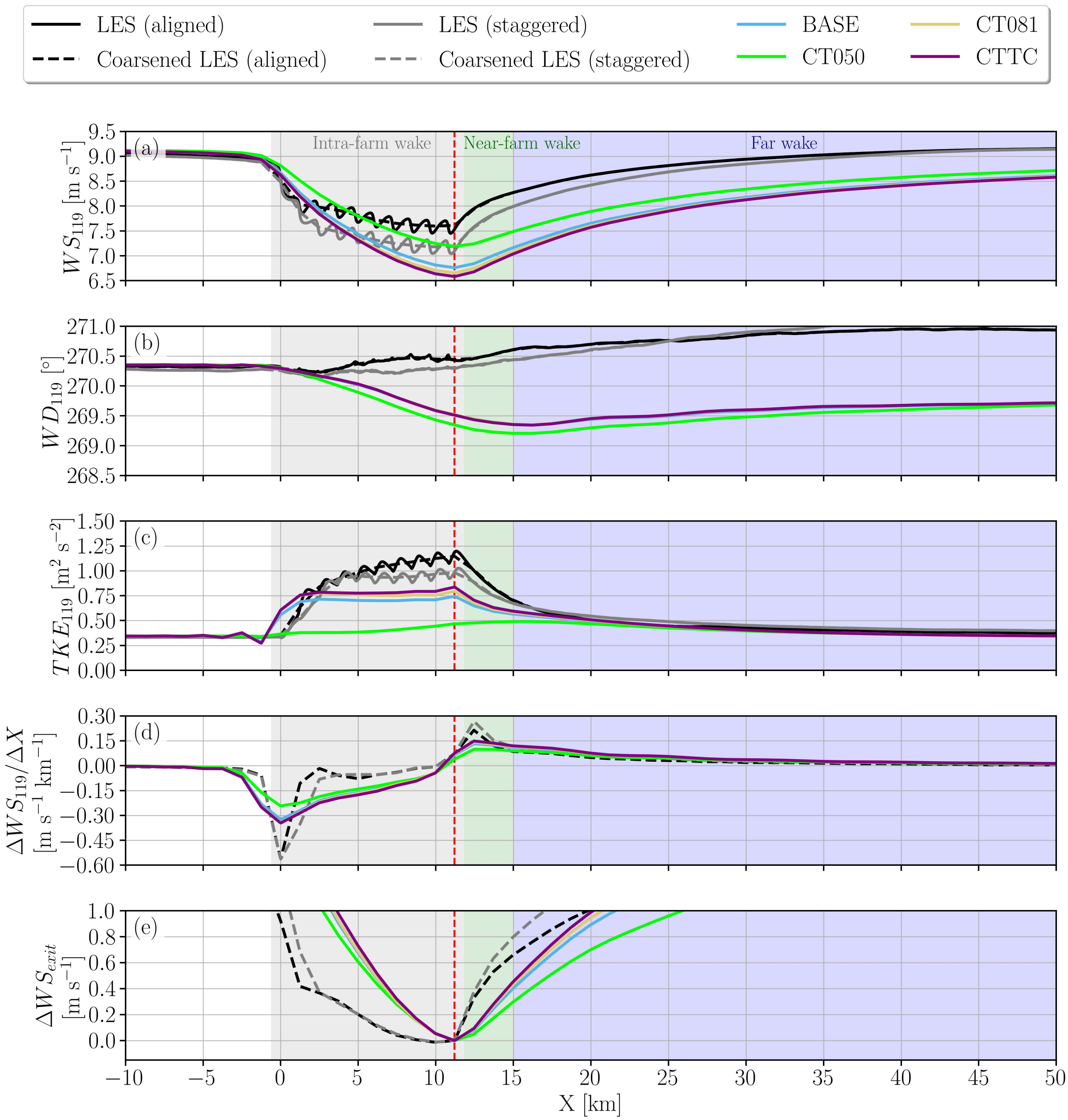

Figure A2. Streamwise variation of spanwise averages over the wind farm area of hub-height wind speed (a), wind direction (b), TKE (c), streamwise gradient of wind speed (d) and wind speed change relative to the wind farm exit (e) for the aligned and staggered LES at full resolution, coarsened LES, and NWP-WFP cases with different C_T. In the CTTC case, the thrust coefficient C_T varies with wind speed according to the turbine's thrust curve. The colored background areas indicate the streamwise extent of the intra-farm wake (gray), near-farm wake (green), and far wake of the farm (blue). The red vertical dashed line marks the wind farm exit.

diagnostics used to characterize intra-farm, near-farm, and far-wake behavior. Buoyancy production and vertical transport are omitted, as their contributions are small relative to the dominant terms and do not influence the conclusions discussed below.

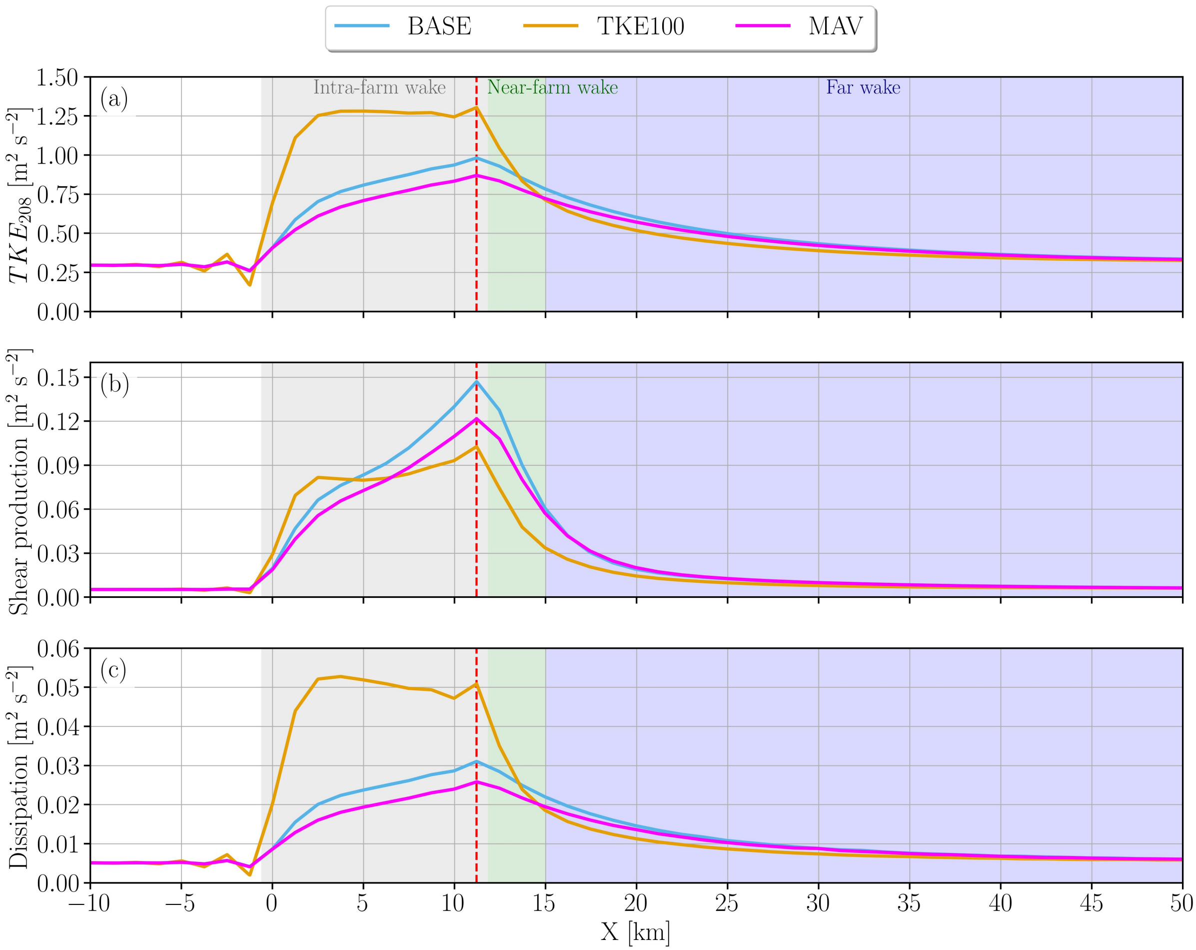

Figure B1. Streamwise variation of spanwise averages over the wind farm area of rotor top tip TKE (a), shear production (b), and dissipation (c) for the BASE, TKE100 and MAV cases. The colored background areas indicate the streamwise extent of the intra-farm wake (gray), near-farm wake (green), and far wake of the farm (blue). The red vertical dashed line marks the wind farm exit.

Figure B1a shows that the TKE is highest within the wind farm due to direct addition by the WFPs, with dissipation (Fig. B1c) closely following the TKE magnitude. Shear production (Fig. B1b) increases through the intra-farm region as the wind speed deficit builds across successive turbine rows (Fig. 7a). In the near-farm wake, where the WFPs are inactive, shear production in the BASE and MAV cases exceeds that of the TKE100 case, despite similar TKE and dissipation levels at the wind-farm exit. This difference is critical: the reduced shear production in TKE100 leads to a reduced TKE in the near-farm wake compared to BASE and MAV. Consistently, cases with larger wind speed deficits exhibit stronger shear production, with the ordering at the farm exit being BASE, followed by MAV and TKE100. These results reinforce the conclusion from Section 4.1 that insufficiently sustained shear production limits TKE levels and eddy viscosity in the near-farm wake of mesoscale NWP-WFP simulations.

Author contributions. Conceptualization: WCR and JKL. Methodology: WCR. Data curation: WCR and JHK. Formal analysis: WCR. Investigation: WCR and JKL. Writing (original draft): WCR and JKL. Writing (review and editing): all authors. All authors contributed to the discussion and interpretation of results.

Competing interests. At least one of the (co-)authors is a member of the editorial board of *Wind Energy Science*.

Acknowledgements. This work was partially supported by the U.S. Department of Energy, Office of Science Energy Earthshot Initiative, as part of the Addressing Challenges in Energy—Floating Wind in a Changing Climate (ACE-FWICC) Energy Earthshot Research Center. A portion of the research (WRF simulations) was performed using computational resources sponsored by the Department of Energy's Office of Critical Minerals and Energy Innovation Wind Energy Technologies Office and located at the National Laboratory of the Rockies. This work was authored in part by the National Laboratory of the Rockies operated for the U.S. Department of Energy (DOE) under Contract No. DE-AC36-08GO28308. This project has received funding from the European Research Council Horizon Europe program (Grant No. 101124815).

References

Abkar, M. and Porté-Agel, F.: Influence of atmospheric stability on wind-turbine wakes: A large-eddy simulation study, Phys. Fluids, 27, https://doi.org/10.1063/1.4913695, 2015.

Abkar, M. and Porté-Agel, F.: A new wind-farm parameterization for large-scale atmospheric models, J. Renew. Sustain. Energy, 7, 1–13, https://doi.org/10.1063/1.4907600, 2015.

Abkar, M., Bae, H. J., and Moin, P.: Minimum-dissipation scalar transport model for large-eddy simulation of turbulent flows, Phys. Rev. Fluids, 1, 041 701, https://doi.org/10.1103/PhysRevFluids.1.041701, 2016a.

Abkar, M., Sharifi, A., and Porté-Agel, F.: Wake flow in a wind farm during a diurnal cycle, J. Turb., 17, 420–441, https://doi.org/10.1080/14685248.2015.1127379, 2016b.

Adams, A. S. and Keith, D. W.: Are global wind power resource estimates overstated?, Environ. Res. Lett., 8, https://doi.org/10.1088/1748-9326/8/1/015021, 2013.

Agarwal, N. J., Lundquist, J. K., Juliano, T. W., and Rybchuk, A.: A North Sea in situ evaluation of the Fitch wind farm parametrization within the Mellor – Yamada – Nakanishi – Niino and 3D planetary boundary layer schemes, Wind Energ. Sci. Discuss., https://doi.org/10.5194/wes-2025-16, 2025.

Albertson, J. D. and Parlange, M. B.: Surface length scales and shear stress: Implications for land-atmosphere interaction over complex terrain, Water Resources Research, 35, 2121–2132, https://doi.org/10.1029/1999WR900094, 1999.

Ali, K., Schultz, D. M., Revell, A., Stallard, T., and Ouro, P.: Assessment of Five Wind-Farm Parameterizations in the Weather Research and Forecasting Model: A Case Study of Wind Farms in the North Sea, Mon. Weather Rev., 151, 2333–2359, https://doi.org/10.1175/MWR-D-23-0006.1, 2023.

Allaerts, D. and Meyers, J.: Boundary-layer development and gravity waves in conventionally neutral wind farms, J. Fluid Mech., 814, 95–130, https://doi.org/10.1017/jfm.2017.11, 2017.

Archer, C. L., Wu, S., Ma, Y., and Jiménez, P. A.: Two corrections for turbulent kinetic energy generated by wind farms in the WRF model, Mon. Weather Rev., 148, 4823–4835, https://doi.org/10.1175/MWR-D-20-0097.1, 2020.

Baidya Roy, S., Pacala, S. W., and Walko, R. L.: Can large wind farms affect local meteorology?, J. Geophys. Res. Atmos., 109, 1–6, https://doi.org/10.1029/2004JD004763, 2004.

Bak, C., Zahle, F., Bitsche, R., Kim, T., Yde, A., Henriksen, L. C., Hansen, M. H., Blasques, J. P. A. A., Gaunaa, M., and Natarajan, A.: The DTU 10-MW Reference Wind Turbine, in: Danish Wind Power Research, Roskilde, Denmark, 2013.

Barthelmie, R. J., Frandsen, S. T., Nielsen, M. N., Pryor, S. C., Rethore, P. E., and Jørgensen, H. E.: Modelling and measurements of power losses and turbulence intensity in wind turbine wakes at Middelgrunden offshore wind farm, Wind Energy, 10, 517–528, https://doi.org/10.1002/we.238, 2007.

Barthelmie, R. J., Hansen, K., Frandsen, S. T., Rathmann, O., Schepers, J. G., Schlez, W., Phillips, J., Rados, K., Zervos, A., Politis, E. S., and Chaviaropoulos, P. K.: Modelling and Measuring Flow and Wind Turbine Wakes in Large Wind Farms Offshore, Wind Energy, 12, 431–444, https://doi.org/10.1002/we.348, 2009.

Blahak, U., Goretzki, B., and Meis, J.: A simple parameterization of drag forces induced by large wind farms for numerical weather prediction models, in: Proceedings of European wind energy conference and exhibition, 1, pp. 4577–4585, 2010.

Bodini, N., Zardi, D., and Lundquist, J. K.: Three-dimensional structure of wind turbine wakes as measured by scanning LiDAR, Atmos. Meas. Tech., 10, 2881–2896, https://doi.org/10.5194/amt-10-2881-2017, 2017.

Bodini, N., Lundquist, J. K., and Kirincich, A.: U.S. East coast LiDAR measurements show offshore wind turbines will encounter very low atmospheric turbulence, Geophys. Res. Lett., 46, 5582–5591, https://doi.org/10.1029/2019GL082636, 2019.

Boettcher, M., Hoffmann, P., Lenhart, H. J., Schlünzen, K. H., and Schoetter, R.: Influence of large offshore wind farms on North German climate, Meteorol. Z., 24, 465–480, https://doi.org/10.1127/metz/2015/0652, 2015.

Boussinesq, M. J.: Théorie de l'écoulement tourbillonnant et tumultueux des liquides, Gauthier-Villars et fils, Paris, France, https://archive.org/details/thbeoriedelbeco01bousrich/page/1/, 1897.

Cal, R. B., Lebrón, J., Castillo, L., Kang, H. S., and Meneveau, C.: Experimental study of the horizontally averaged flow structure in a model wind-turbine array boundary layer, J. Renew. Sustain. Energy, 2, 0–25, https://doi.org/10.1063/1.3289735, 2010.

Calaf, M., Meneveau, C., and Meyers, J.: Large eddy simulations of fully developed wind-turbine array boundary layers, Phys. Fluids, 22, 015 110, https://doi.org/10.1063/1.3291077, 2010.

Cañadillas, B., Foreman, R., Barth, V., Siedersleben, S., Lampert, A., Platis, A., Djath, B., Schulz-Stellenfleth, J., Bange, J., Emeis, S., and Neumann, T.: Offshore wind farm wake recovery: Airborne measurements and its representation in engineering models, Wind Energy, 23, 1249–1265, https://doi.org/10.1002/we.2484, 2020.

Englberger, A., Lundquist, J. K., and Dörnbrack, A.: Changing the rotational direction of a wind turbine under veering inflow: a parameter study, Wind Energ. Sci., 5, 1623–1644, https://doi.org/10.5194/wes-5-1623-2020, 2020.

Eriksson, O., Lindvall, J., Breton, S. P., and Ivanell, S.: Wake downstream of the Lillgrund wind farm - A comparison between LES using the actuator disc method and a wind farm parametrization in WRF, J. Phys. Conf. Ser., 625, https://doi.org/10.1088/1742-6596/625/1/012028, 2015.

Fischereit, J., Brown, R., Larsén, X. G., Badger, J., and Hawkes, G.: Review of mesoscale Wind-Farm Parametrizations and their applications, Bound.-Layer Meteorol., 182, 175–224, https://doi.org/10.1007/s10546-021-00652-y, 2022a.

Fischereit, J., Schaldemose Hansen, K., Larsén, X. G., van der Laan, M. P., Réthoré, P. E., and Murcia Leon, J. P.: Comparing and validating intra-farm and farm-to-farm wakes across different mesoscale and high-resolution wake models, Wind Energ. Sci., 7, 1069–1091, https://doi.org/10.5194/wes-7-1069-2022, 2022b.

Fitch, A. C., Olson, J. B., Lundquist, J. K., Dudhia, J., Gupta, A. K., Michalakes, J., and Barstad, I.: Local and mesoscale impacts of wind farms as parameterized in a mesoscale NWP model, Mon. Weather Rev., 140, 3017–3038, https://doi.org/10.1175/MWR-D-11-00352.1, 2012.

Fitch, A. C., Lundquist, J. K., and Olson, J. B.: Mesoscale influences of wind farms throughout a diurnal cycle, Mon. Weather Rev., 141, 2173–2198, https://doi.org/10.1175/MWR-D-12-00185.1, 2013a.

Fitch, A. C., Olson, J. B., and Lundquist, J. K.: Parameterization of Wind Farms in Climate Models, J. Climate, 26, 6439–6458, https://doi.org/10.1175/JCLI-D-12-00376.1, 2013b.

Gadde, S. N. and Stevens, R. J. A. M.: Effect of Coriolis force on a wind farm wake, J. Phys. Conf. Ser., 1256, 012 026, https://doi.org/10.1088/1742-6596/1256/1/012026, 2019.

Gadde, S. N., Stieren, A., and Stevens, R. J. A. M.: Large-Eddy Simulations of Stratified Atmospheric Boundary Layers: Comparison of Different Subgrid Models, Bound.-Layer Meteorol., 178, 363–382, https://doi.org/10.1007/s10546-020-00570-5, 2021.

García-Santiago, O., Hahmann, A. N., Badger, J., and Peña, A.: Evaluation of wind farm parameterizations in the WRF model under different atmospheric stability conditions with high-resolution wake simulations, Wind Energ. Sci., 9, 963–979, https://doi.org/10.5194/wes-9-963-2024, 2024.

Haupt, S. E., Kosovic, B., Shaw, W., Berg, L. K., Churchfield, M., Cline, J., Draxl, C., Ennis, B., Koo, E., Kotamarthi, R., Mazzaro, L., Mirocha, J., Moriarty, P., Muñóz-Esparza, D., Quon, E., Rai, R. K., Robinson, M., and Sever, G.: On bridging a modeling scale gap: mesoscale to microscale coupling for wind energy, Bull. Am. Meteorol. Soc., 100, 2533–2550, https://doi.org/10.1175/bams-d-18-0033.1, 2019.

Haupt, S. E., Kosović, B., Berg, L. K., Kaul, C. M., Churchfield, M., Mirocha, J., Allaerts, D., Brummet, T., Davis, S., DeCastro, A., Dettling, S., Draxl, C., Gagne, D. J., Hawbecker, P., Jha, P., Juliano, T., Lassman, W., Quon, E., Rai, R. K., Robinson, M., Shaw, W., and Thedin, R.: Lessons learned in coupling atmospheric models across scales for onshore and offshore wind energy, Wind Energ. Sci., 8, 1251–1275, https://doi.org/10.5194/wes-8-1251-2023, 2023.

Hsieh, A. S., Cheung, L. C., Blaylock, M. L., Brown, K. A., Houck, D. R., Herges, T. G., DeVelder, N. B., Maniaci, D. C., Yalla, G. R., Sakievich, P. J., Radunz, W. C., and Carmo, B. S.: Model intercomparison of the ABL, turbines, and wakes within the AWAKEN wind farms under neutral stability conditions, J. Renew. Sustain. Energy, 17, https://doi.org/10.1063/5.0211729, 2025.

Iungo, G. V., Wu, Y. T., and Porté-Agel, F.: Field measurements of wind turbine wakes with LiDARs, J. Atmos. Ocean. Technol., 30, 274–287, https://doi.org/10.1175/JTECH-D-12-00051.1, 2013.

Ivanova, L. A. and Nadyozhina, E. D.: Numerical simulation of wind farm influence on wind flow, Wind Engineering, 24, 257–269, https://doi.org/10.1260/0309524001495620, 2000.

Jimenez, A., Crespo, A., Migoya, E., and Garcia, J.: Large-eddy simulation of spectral coherence in a wind turbine wake, Environ. Res. Lett., 3, 015 004, https://doi.org/10.1088/1748-9326/3/1/015004, 2008.

Juliano, T. W., Kosović, B., Jiménez, P. A., Eghdami, M., Haupt, S. E., and Martilli, A.: "Gray Zone" simulations using a three-dimensional planetary boundary layer parameterization in the Weather Research and Forecasting model, Mon. Weather Rev., 150, 1585–1619, https://doi.org/10.1175/MWR-D-21-0164.1, 2022.

Kasper, J. H. and Stevens, R. J. A. M.: From turbine-scale to wind farm-scale wake recovery: Understanding the transition, J. Renew. Sustain. Energy, 18, 1–21, https://doi.org/10.1063/5.0285347, 2026.

Kasper, J. H., Stieren, A., and Stevens, R. J. A. M.: Simulation and modeling of wind farms in baroclinic atmospheric boundary layers, J. Renew. Sustain. Energy, 16, 1–15, https://doi.org/10.1063/5.0220322, 2024.

Keith, D. W., DeCarolis, J. F., Denkenberger, D. C., Lenschow, D. H., Malyshev, S. L., Pacala, S., and Rasch, P. J.: The influence of large-scale wind power on global climate, Proc. Natl. Acad. Sci. U.S.A., 101, 16 115–16 120, https://doi.org/10.1073/pnas.0406930101, 2004.

Khanjari, A., Feroz, A., and Archer, C. L.: An analytical formulation for turbulent kinetic energy added by wind turbines based on large-eddy simulation, Wind Energ. Sci., 10, 887–905, https://doi.org/10.5194/wes-2024-128, 2025.

Kosović, B., Munoz, P. J., Juliano, T. W., Martilli, A., Eghdami, M., Barros, A. P., and Haupt, S. E.: Three-dimensional planetary boundary layer parameterization for high-resolution mesoscale simulations, J. Phys. Conf. Ser., 1452, 012 080, https://doi.org/10.1088/1742-6596/1452/1/012080, 2020.

Lanzilao, L. and Meyers, J.: Wind-farm wake recovery mechanisms in conventionally neutral boundary layers, Journal of Fluid Mechanics, 1015, A5, https://doi.org/10.1017/jfm.2025.10320, 2025.

Larsén, X. G. and Fischereit, J.: A case study of wind farm effects using two wake parameterizations in the Weather Research and Forecasting (WRF) model (V3.7.1) in the presence of low-level jets, Geosci. Model Dev., 14, 3141–3158, https://doi.org/10.5194/gmd-14-3141-2021, 2021.

Lee, J. C. Y. and Lundquist, J. K.: Evaluation of the wind farm parameterization in the Weather Research and Forecasting model (version 3.8.1) with meteorological and turbine power data, Geosci. Model Dev., 10, 4229–4244, https://doi.org/10.5194/gmd-10-4229-2017, 2017.

Lundquist, J. K., DuVivier, K. K., Kaffine, D., and Tomaszewski, J. M.: Costs and consequences of wind turbine wake effects arising from uncoordinated wind energy development, Nat. Energy, 4, 26–34, https://doi.org/10.1038/s41560-018-0281-2, 2019.

Ma, Y., Archer, C. L., and Vasel-Be-Hagh, A.: The Jensen wind farm parameterization, Wind Energy Science, 7, 2407–2431, https://doi.org/10.5194/wes-7-2407-2022, 2022a.

Ma, Y., Archer, C. L., and Vasel-Be-Hagh, A.: Comparison of individual versus ensemble wind farm parameterizations inclusive of sub-grid wakes for the WRF model, Wind Energy, 25, 1573–1595, https://doi.org/10.1002/we.2758, 2022b.

Magnusson, M. and Smedman, A. S.: Influence of atmospheric stability on wind turbine wakes, Wind Eng., 18, 139–152, http://www.jstor.org/stable/43749538, 1994.

Malyshev, S. L., Pacala, S. W., Keith, D. W., Denkenberger, D. C., Baidya Roy, S., and Shevliakova, E.: Climate response to large-scale wind farms, in: AGU Fall Meeting Abstracts, vol. 2003, pp. A31E–0104, 2003.

Mangara, R. J., Guo, Z., and Li, S.: Performance of the wind farm parameterization scheme coupled with the weather research and forecasting model under multiple resolution regimes for simulating an onshore wind farm, Adv. Atmos. Sci., 36, 119–132, https://doi.org/10.1007/s00376-018-8028-3, 2019.

Mellor, G. L. and Yamada, T.: Development of a turbulence closure model for geophysical fluid problems, Rev. Geophys., 20, 851–875, https://doi.org/10.1029/RG020i004p00851, 1982.

Mirocha, J. D., Rajewski, D. A., Marjanovic, N., Lundquist, J. K., Kosović, B., Draxl, C., and Churchfield, M. J.: Investigating wind turbine impacts on near-wake flow using profiling LiDAR data and large-eddy simulations with an actuator disk model, J. Renew. Sustain. Energy, 7, https://doi.org/10.1063/1.4928873, 2015.

Mirocha, J. D., Churchfield, M. J., Muñoz-Esparza, D., Rai, R. K., Feng, Y., Kosović, B., Haupt, S. E., Brown, B., Ennis, B. L., Draxl, C., Rodrigo, J. S., Shaw, W. J., Berg, L. K., Moriarty, P. J., Linn, R. R., Kotamarthi, V. R., Balakrishnan, R., Cline, J. W., Robinson, M. C., and Ananthan, S.: Large-eddy simulation sensitivities to variations of configuration and forcing parameters in canonical boundary-layer flows for wind energy applications, Wind Energ. Sci., 3, 589–613, https://doi.org/10.5194/wes-3-589-2018, 2018.

Montavon, C., Rodaway, C., Gunn, K., Smith, G., Dunsmore, D., Hoyo, M. D., and Sinclair, K.: Cluster wakes and their effect on a wind farm annual energy production, Tech. Rep. 1, DNV-RWE, Whitepaper, 2024.

Nakanishi, M. and Niino, H.: Development of an Improved Turbulence Closure Model for the Atmospheric Boundary Layer, J. Meteorol. Soc. Jpn., 87, 895–912, https://doi.org/10.2151/jmsj.87.895, 2009.

Olson, J. B., Angevine, W. M., Turner, D. D., Sun, X., Simonson, J. M., Evans, C., Kenyon, J. S., Li, H., Schnell, J., Puhales, F. S., Cherubini, T., Li, W., and Zhang, M.: A Description of the MYNN-EDMF Turbulence Scheme, Tech. Rep. NOAA Technical Memorandum OAR GSL-77, NOAA Global Systems Laboratory, https://doi.org/10.25923/rahr-sj70, 2026.

Ouro, P., Ghobrial, M., Ali, K., and Stallard, T.: Numerical modelling of offshore wind farm cluster wakes, Renew. Sustain. Energy Rev., 215, 115 526, https://doi.org/10.1016/j.rser.2025.115526, 2025.

Pan, Y. and Archer, C. L.: A hybrid wind-farm parametrization for mesoscale and climate models, Bound.-Layer Meteorol., 168, 469–495, https://doi.org/10.1007/s10546-018-0351-9, 2018.

Peña, A., Mirocha, J. D., and van der Laan, M. P.: Evaluation of the Fitch Wind-Farm Wake Parameterization with Large-Eddy Simulations of Wakes Using the Weather Research and Forecasting Model, Mon. Weather Rev., 150, 3051–3064, https://doi.org/10.1175/MWR-D-22-0118.1, 2022.

Peña, A., Kosović, B., and Mirocha, J. D.: Evaluation of idealized large-eddy simulations performed with the Weather Research and Forecasting model using turbulence measurements from a 250 m meteorological mast, Wind Energ. Sci., 6, 645–661, https://doi.org/10.5194/wes-6-645-2021, 2021.

Platis, A., Siedersleben, S. K., Bange, J., Lampert, A., Bärfuss, K., Hankers, R., Cañadillas, B., Foreman, R., Schulz-Stellenfleth, J., Djath, B., Neumann, T., and Emeis, S.: First in situ evidence of wakes in the far field behind offshore wind farms, Scientific Reports, 8, 1–10, https://doi.org/10.1038/s41598-018-20389-y, 2018.

Porté-Agel, F., Bastankhah, M., and Shamsoddin, S.: Wind-Turbine and Wind-Farm Flows: A Review, Bound.-Layer Meteorol., 174, 1–59, https://doi.org/10.1007/s10546-019-00473-0, 2020.

Pryor, S. C. and Barthelmie, R. J.: Power production, inter- and intra-array wake losses from the U.S. East coast offshore wind energy lease areas, Energies, 17, https://doi.org/10.3390/en17051063, 2024.

Pryor, S. C., Shepherd, T. J., Volker, P. J., Hahmann, A. N., and Barthelmie, R. J.: "Wind Theft" from onshore wind turbine arrays: Sensitivity to wind farm parameterization and resolution, J. Appl. Meteorol. Climatol., 59, 153–174, https://doi.org/10.1175/JAMC-D-19-0235.1, 2020.

Quint, D., Lundquist, J. K., Bodini, N., and Rosencrans, D.: Simulated meteorological impacts of offshore wind turbines and sensitivity to the amount of added turbulence kinetic energy, Wind Energ. Sci., 10, 1269–1301, https://doi.org/10.5194/wes-10-1269-2025, 2025.

Radünz, W. C.: NWP-WFP simulation setup of an idealized offshore wind farm in near-neutral conditions, https://doi.org/10.5281/zenodo.15925137, 2025.

Rai, R. K., Berg, L. K., Kosović, B., Haupt, S. E., Mirocha, J. D., Ennis, B. L., and Draxl, C.: Evaluation of the impact of horizontal grid spacing in terra incognita on coupled mesoscale-microscale simulations using the WRF framework, Mon. Weather Rev., 147, 1007–1027, https://doi.org/10.1175/MWR-D-18-0282.1, 2019.

Redfern, S., Olson, J. B., Lundquist, J. K., and Clack, C. T. M.: Incorporation of the rotor-equivalent wind speed into the weather research and forecasting model's wind farm parameterization, Mon. Weather Rev., 147, 1029–1046, https://doi.org/10.1175/MWR-D-18-0194.1, 2019.

Rosencrans, D., Lundquist, J. K., Optis, M., Rybchuk, A., Bodini, N., and Rossol, M.: Seasonal variability of wake impacts on US mid-Atlantic offshore wind plant power production, Wind Energ. Sci., 9, 555–583, https://doi.org/10.5194/wes-9-555-2024, 2024.

Rozema, W., Bae, H. J., Moin, P., and Verstappen, R.: Minimum-dissipation models for large-eddy simulation, Phys. Fluids, 27, https://doi.org/10.1063/1.4928700, 2015.

Rybchuk, A., Juliano., T. W., Lundquist, J. K., Rosencrans, D., Bodini, N., and Optis, M.: The sensitivity of the fitch wind farm parameterization to a three-dimensional planetary boundary layer scheme, Wind Energ. Sci., 7, 2085–2098, https://doi.org/10.5194/wes-7-2085-2022, 2022.

Sanchez Gomez, M., Deskos, G., Lundquist, J. K., and Juliano, T. W.: Can mesoscale models capture the effect from cluster wakes offshore?, J. Phys. Conf. Ser., 2767, https://doi.org/10.1088/1742-6596/2767/6/062013, 2024.

Shepherd, T. J., Barthelmie, R. J., and Pryor, S. C.: Sensitivity of wind turbine array downstream effects to the parameterization used in WRF, J. Appl. Meteorol. Climatol., 59, 333–361, https://doi.org/10.1175/JAMC-D-19-0135.1, 2020.

Siedersleben, S. K., Lundquist, J. K., Platis, A., Bange, J., Bärfuss, K., Lampert, A., Cañadillas, B., Neumann, T., and Emeis, S.: Micrometeorological impacts of offshore wind farms as seen in observations and simulations, Environ. Res. Lett., 13, https://doi.org/10.1088/1748-9326/aaea0b, 2018a.

Siedersleben, S. K., Platis, A., Lundquist, J. K., Lampert, A., Bärfuss, K., Cañadillas, B., Djath, B., Schulz-Stellenfleth, J., Bange, J., Neumann, T., and Emeis, S.: Evaluation of a Wind Farm Parametrization for Mesoscale Atmospheric Flow Models with Aircraft Measurements, Meteorol. Z., 27, 401–415, https://doi.org/10.1127/metz/2018/0900, 2018b.

Siedersleben, S. K., Platis, A., Lundquist, J. K., Djath, B., Lampert, A., Bärfuss, K., Cañadillas, B., Schulz-Stellenfleth, J., Bange, J., Neumann, T., and Emeis, S.: Turbulent kinetic energy over large offshore wind farms observed and simulated by the mesoscale model WRF (3.8.1), Geosci. Model Dev., 13, 249–268, https://doi.org/10.5194/gmd-13-249-2020, 2020.

Skamarock, W. C., Klemp, J. B., Dudhi, J., Gill, D. O., Barker, D. M., Duda, M. G., Huang, X.-Y., Wang, W., and Powers, J. G.: A Description of the Advanced Research WRF Version 4. Tech. Note NCAR TN-475+STR, Tech. rep., University Corporation for Atmospheric Research, ISBN NCAR/TN–468+STR, https://doi.org/10.5065/D6DZ069T, 2019.

Stevens, R. J. A. M. and Meneveau, C.: Flow structure and turbulence in wind farms, Annu. Rev. Fluid Mech., 49, 311–339, https://doi.org/10.1146/annurev-fluid-010816-060206, 2017.

Stevens, R. J. A. M., Graham, J., and Meneveau, C.: A concurrent precursor inflow method for Large Eddy Simulations and applications to finite length wind farms, Renewable Energy, 68, 46–50, https://doi.org/10.1016/j.renene.2014.01.024, 2014.

Stieren, A. and Stevens, R. J. A. M.: Impact of wind farm wakes on flow structures in and around downstream wind farms, Flow, 2, https://doi.org/10.1017/flo.2022.15, 2022.

Stieren, A., Kasper, J. H., Gadde, S. N., and Stevens, R. J. A. M.: Impact of negative geostrophic wind shear on wind farm performance, PRX Energy, 1, 1, https://doi.org/10.1103/prxenergy.1.023007, 2022.

Stipa, S., Ajay, A., and Brinkerhoff, J.: The actuator farm model for large eddy simulation (LES) of wind-farm-induced atmospheric gravity waves and farm-farm interaction, Wind Energ. Sci., 9, 2301–2332, https://doi.org/10.5194/wes-9-2301-2024, 2024.

Stull, R. B.: An introduction to boundary layer meteorology, Kluwer Academic Publishers, The Netherlands, 1988.

Tomaszewski, J. M. and Lundquist, J. K.: Simulated wind farm wake sensitivity to configuration choices in the Weather Research and Forecasting model version 3.8.1, Geosci. Model Dev., 13, 2645–2662, https://doi.org/10.5194/gmd-13-2645-2020, 2020.

van der Laan, M. P. and Sørensen, N. N.: Why the Coriolis force turns a wind farm wake clockwise in the Northern Hemisphere, Wind Energ. Sci., 2, 285–294, https://doi.org/10.5194/wes-2-285-2017, 2017.

van der Laan, M. P., Baungaard, M., and Kelly, M.: Brief communication: A clarification of wake recovery mechanisms, Wind Energ. Sci., 8, 247–254, https://doi.org/10.5194/wes-8-247-2023, 2023.

van Stratum, B., Theeuwes, N., Barkmeijer, J., van Ulft, B., and Wijnant, I.: A One-Year-Long Evaluation of a Wind-Farm Parameterization in HARMONIE-AROME, Journal of Advances in Modeling Earth Systems, 14, https://doi.org/10.1029/2021MS002947, 2022.

Vanderwende, B. J., Kosović, B., Lundquist, J. K., and Mirocha, J. D.: Simulating effects of a wind-turbine array using LES and RANS, J. Adv. Model. Earth Syst., 8, 1376–1390, https://doi.org/10.1002/2016MS000652, 2016.

Veers, P., Dykes, K., Lantz, E., Barth, S., Bottasso, C. L., Carlson, O., Clifton, A., Green, J., Green, P., Holttinen, H., Laird, D., Lehtomäki, V., Lundquist, J. K., Manwell, J., Marquis, M., Meneveau, C., Moriarty, P., Munduate, X., Muskulus, M., Naughton, J., Pao, L., Paquette, J., Peinke, J., Robertson, A., Rodrigo, J. S., Sempreviva, A. M., Smith, J. C., Tuohy, A., and Wiser, R.: Grand challenges in the science of wind energy, Science, 366, https://doi.org/10.1126/science.aau2027, 2019.

Veers, P., Dykes, K., Basu, S., Bianchini, A., Clifton, A., Green, P., Holttinen, H., Kitzing, L., Kosovic, B., Lundquist, J. K., Meyers, J., O'Malley, M., Shaw, W. J., and Straw, B.: Grand Challenges: wind energy research needs for a global energy transition, Wind Energ. Sci., 7, 2491–2496, https://doi.org/10.5194/wes-7-2491-2022, 2022.

Vermeer, L. J., Sørensen, J. N., and Crespo, A.: Wind turbine wake aerodynamics, Prog. Aerosp. Sci., 39, 467–510, https://doi.org/10.1016/S0376-0421(03)00078-2, 2003.

Volker, P. J. H., Badger, J., Hahmann, A. N., and Ott, S.: The explicit wake parametrisation V1.0: A wind farm parametrisation in the mesoscale model WRF, Geosci. Model Dev., 8, 3715–3731, https://doi.org/10.5194/gmd-8-3715-2015, 2015.

Vollmer, L., Sengers, B. A. M., and Dörenkämper, M.: Brief communication: A simple axial induction modification to the Weather Research and Forecasting Fitch wind farm parameterization, Wind Energ. Sci., 9, 1689–1693, https://doi.org/10.5194/wes-9-1689-2024, 2024.

Wang, C. and Prinn, R. G.: Potential climatic impacts and reliability of very large-scale wind farms, Atmos. Chem. Phys., 10, 2053–2061, https://doi.org/10.5194/acp-10-2053-2010, 2010.

Wyngaard, J. C.: Toward numerical modeling in the "Terra Incognita", J. Atmos. Sci., 61, 1816–1826, https://doi.org/10.1175/1520-0469(2004)061<1816:TNMITT>2.0.CO;2, 2004.

Xie, S. and Archer, C.: Self-similarity and turbulence characteristics of wind turbine wakes via large-eddy simulation, Wind Energy, 18, 1815–1838, https://doi.org/10.1002/we.1792, 2015.